Neonatal Apex Resection Triggers Cardiomyocyte Proliferation, Neovascularization and Functional Recovery Despite Local Fibrosis

Vasco Sampaio-Pinto,[1,2,3] Sílvia C. Rodrigues,[1,2] Tiago L. Laundos,[1,2,3] Elsa D. Silva,[1,2] Francisco Vasques-Nóvoa,[1,2,4] Ana C. Silva,[1,2,3,5] Rui J. Cerqueira,[4] Tatiana P. Resende,[1,2] Nicola Pianca,[6] Adelino Leite-Moreira,[4] Gabriele D'Uva,[6] Sólveig Thorsteinsdóttir,[7] Perpétua Pinto-do-Ó,[1,2,3,8] and Diana S. Nascimento[1,2,8,*]

[1]i3S - Instituto de Investigação e Inovação em Saúde, Universidade do Porto, Rua Alfredo Allen 208, 4200-135 Porto, Portugal
[2]INEB - Instituto Nacional de Engenharia Biomédica, Universidade do Porto, Rua Alfredo Allen 208, 4200-135 Porto, Portugal
[3]ICBAS - Instituto de Ciências Biomédicas de Abel Salazar, Universidade do Porto, Rua Jorge Viterbo Ferreira 228, 4050-313 Porto, Portugal
[4]Departamento de Fisiologia e Cirurgia Cardiotorácica, Faculdade de Medicina da Universidade do Porto, Rua Doutor Plácido da Costa, 4200-450 Porto, Portugal
[5]Gladstone Institutes, University of California San Francisco, San Francisco 94158, USA
[6]Scientific and Technological Pole, IRCCS MultiMedica, 20138 Milan, Italy
[7]Departamento de Biologia Animal, cE3c - Centro de Ecologia, Evolução e Alterações Ambientais, Faculdade de Ciências, Universidade de Lisboa, Campo Grande 1749-016, Lisboa, Portugal
[8]Co-senior author
*Correspondence: dsn@ineb.up.pt
https://doi.org/10.1016/j.stemcr.2018.01.042

SUMMARY

So far, opposing outcomes have been reported following neonatal apex resection in mice, questioning the validity of this injury model to investigate regenerative mechanisms. We performed a systematic evaluation, up to 180 days after surgery, of the pathophysiological events activated upon apex resection. In response to cardiac injury, we observed increased cardiomyocyte proliferation in remote and apex regions, neovascularization, and local fibrosis. In adulthood, resected hearts remain consistently shorter and display permanent fibrotic tissue deposition in the center of the resection plane, indicating limited apex regrowth. However, thickening of the left ventricle wall, explained by an upsurge in cardiomyocyte proliferation during the initial response to injury, compensated cardiomyocyte loss and supported normal systolic function. Thus, apex resection triggers both regenerative and reparative mechanisms, endorsing this injury model for studies aimed at promoting cardiomyocyte proliferation and/or downplaying fibrosis.
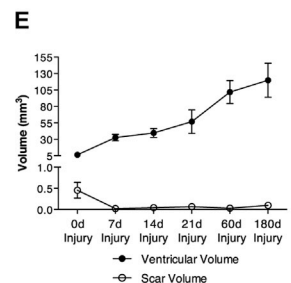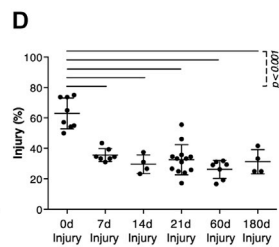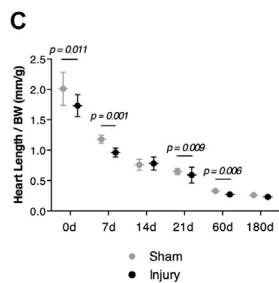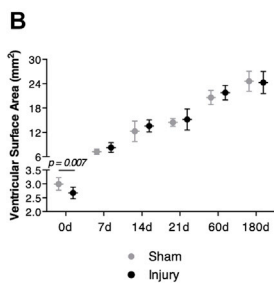
INTRODUCTION

Cardiovascular diseases are the leading cause of death worldwide (Mozaffarian et al., 2016), which is largely attributed to the limited regenerative capacity of the mammalian heart. However, this paradigm has been challenged by studies describing a developmental window for heart regeneration in mammals. Although the first reference to mammalian heart regeneration was provided by Mario Robledo in 1956 (Robledo, 1956), this concept only became robustly supported in 2011 after Sadek and colleagues demonstrated that murine hearts, when subjected to apex resection during the first day of life, were able to reestablish the myocardial tissue through activation of cardiomyocyte (CM) proliferation (Porrello et al., 2011). This report proposed that, like lower vertebrates (Flink, 2002; Poss et al., 2002), the mammalian heart holds an intrinsic ability to regenerate from injury, which could be exploited for therapeutic purposes. This work also set the stage for several studies identifying regulators of CM proliferation (Aurora et al., 2014; Bassat et al., 2017; D'Uva et al., 2015; Heallen et al., 2013; Mahmoud et al., 2013) or describing distinct injury models (Darehzereshki et al., 2015; Haubner et al., 2012; Jesty et al., 2012; Lavine et al., 2014; Porrello et al., 2013; Uygur and Lee, 2016).

In 2014, controversy arose when another laboratory, using the same injury model, reported substantial scarring in the resected apex region, which was accompanied by impaired neovascularization and CM proliferation (Andersen et al., 2014a). Further work by this group showed that fibrotic tissue deposition in the resected region was definitive, and that cardiac function was permanently reduced as animals developed dilated cardiomyopathy, with left ventricle (LV) chamber dilation and wall thinning (Andersen et al., 2016).

The reason for these contrasting findings is still unclear (Andersen et al., 2014b; Kotlikoff et al., 2014; Sadek et al., 2014), although technical variations such as injury severity were shown to impact the formation of scar tissue upon apex resection (Bryant et al., 2015) and cryoinjury (Darehzereshki et al., 2015). Thus, the ability of neonatal hearts to regenerate after apex resection seems to be dependent on small technical variations which at present hampers progress in the field.

Additional difficulties are related to the evaluation of the fibrotic scar (Andersen et al., 2014a; Bryant et al., 2015) and the fact that the assessment of CM proliferation, the most important hallmark for cardiac regeneration, is technically

A

0d Injury

21d Injury

21d Sham

60d Injury

60d Sham

180d Injury

180d Sham

A1   A2   A3   A4

B   C   D   E

(legend on next page)

challenging. In particular, CM proliferation in mammals can be easily mistaken for CM binucleation that initiates around birth (reviewed in Zebrowski et al., 2016), an event characterized by karyokinesis without cytokinesis, leading to CM terminal differentiation (Soonpaa et al., 1996). Of note, studies addressing the response to apex resection in neonatal mice have either focused on functional assessment or histopathological alterations (Andersen et al., 2014a), but longitudinal studies examining cardiac remodeling, function, and the precise tissue response to injury have not yet been performed.

Since there are antagonizing reports and because tissue regeneration and repair often activate overlapping mechanisms (Aurora et al., 2014; Tidball, 2011), we evaluated both tissue responses following neonatal apex resection. Hence, a systematic assessment of the pathophysiological events occurring over 180 days after surgery was performed. We found that apex resection triggers both regenerative (e.g. neovascularization and CM proliferation) and reparative (e.g. cardiac fibrosis) mechanisms which result in an adult heart with more CMs, benign adaptive cardiac remodeling and restored systolic function.

RESULTS

Establishment of Neonatal Apex Resection Injury Model

One-day-old (P1) C57BL/6 mice were subjected to apical resection by thoracotomy using the exposure of the LV lumen as a standardized method for resection size (Mahmoud et al., 2014; Porrello et al., 2011). Sham controls underwent the same surgical procedure without resection of the apex (no cardiac manipulation of any kind).

Immediately after the surgical procedure, the survival rate of apex-resected animals was equivalent to sham controls (∼87%). However, maternal cannibalization reduced survival at 24 hr post-surgery to 61% and 82% for injury and sham groups, respectively.

Hearts Are Not Fully Restored at the Histological Level

The ventricular surface area and heart length/body weight ratio were significantly reduced upon apical resection by ∼11% and ∼14%, respectively (Figures 1A–1C), similar to other reports (Andersen et al., 2014a; Porrello et al., 2011). Representative sampling of the heart (Figure S1A) and histological characterization by Masson's trichrome (MT) staining (Figures 1A and S1B) revealed that apex resection induced noticeable cardiac remodeling, with impact on heart morphology and local deposition of fibrotic tissue (Figures 1B–1D). From 7 to 21 days after surgery, apex regrowth was evident as myocardial tissue was observed below the resection site. Alongside, the myocardial tissue in the innermost part of the apex where the lumen was exposed, was surrounded by a subepicardial scar (Figures 1A and S1B). Higher magnification revealed that the scar undergoes a maturation process, which starts with a scattered deposition of collagenous material and matures to a fibrillar appearance, occupying most of the central apex wall from 60 days after resection onward (Figures 1A1–1A4, S1B1, S1B2, and S1C). In contrast, areas surrounding the central apex region displayed myocardial integrity.

Ventricular surface area was restored at 7 days after injury (Figure 1B), and resected hearts weighed the same or were even heavier than intact hearts (Figures S1D and S1E). However, injured hearts were consistently shorter throughout the study, indicating that heart growth was mainly achieved through short-axis expansion (Figure 1C). The extent of injury, estimated by determining the percentage of sections with cardiac damage (i.e., myocardial disruption or cardiac fibrosis), decreased over time, which correlates with an actual reduction in scar volume (Figures 1D and 1E). Overall, these results indicate that resected hearts remain shorter, have permanent scarring, and do not fully regenerate.

### Resected Hearts Are Functionally Competent

Echocardiograms at 21, 60, 120, and 180 days following surgery confirmed that resected ventricles underwent severe morphological alterations (i.e., long-axis shortening and short-axis widening) (Figure 2A). However, in contrast to previous reports (Andersen et al., 2016), our data showed that short-axis expansion occurred due to a thickening of the anterior and posterior wall of the LV (Figures 2B and 2C) and left ventricular chamber dilation (Figure 2D).

Figure 1. Hearts Do Not Fully Regenerate the Resected Apex
(A) Representative MT-stained sections of apex-resected and sham controls following surgery. Sections exhibiting myocardial disruption and/or cardiac fibrosis are highlighted by a dashed line. Scale bars, 2 mm. High-magnification images of the injury site (A1, 0 day; A2, 21 days; A3, 60 days; and A4, 180 days) show collagen (blue staining) from 21 days onward. Scale bars, 250 μm.
(B and C) Ventricular surface area (from left to right, n = 8, 10, 8, 14, 3, 7, 4, 4) (B) and heart length/ body weight (BW) (from left to right, n = 11, 11, 8, 10, 4, 7, 4, 4) (C) of resected and sham-operated hearts were determined in MT-stained paraffin sections at 0, 7, 14, 21, 60, and 180 days post-surgery.
(D and E) Injury extension (from left to right, n = 8, 12, 7, 4) (D) and ventricular and scar volume (from left to right, n = 19, 14, 7, 4) (E) were calculated on MT-stained paraffin sections. All values are presented as means ± SD. See also Figure S1 for representative MT sections at 7 and 14 days after surgery, data on heart weight, heart to BW ratio, and percentage of fibrosis in the apex.

A **180d Sham** **180d Injury**

B

C

D

E

F

G

H

I

J

K

L

Sham
Injury

M

180d Sham **180d Injury**
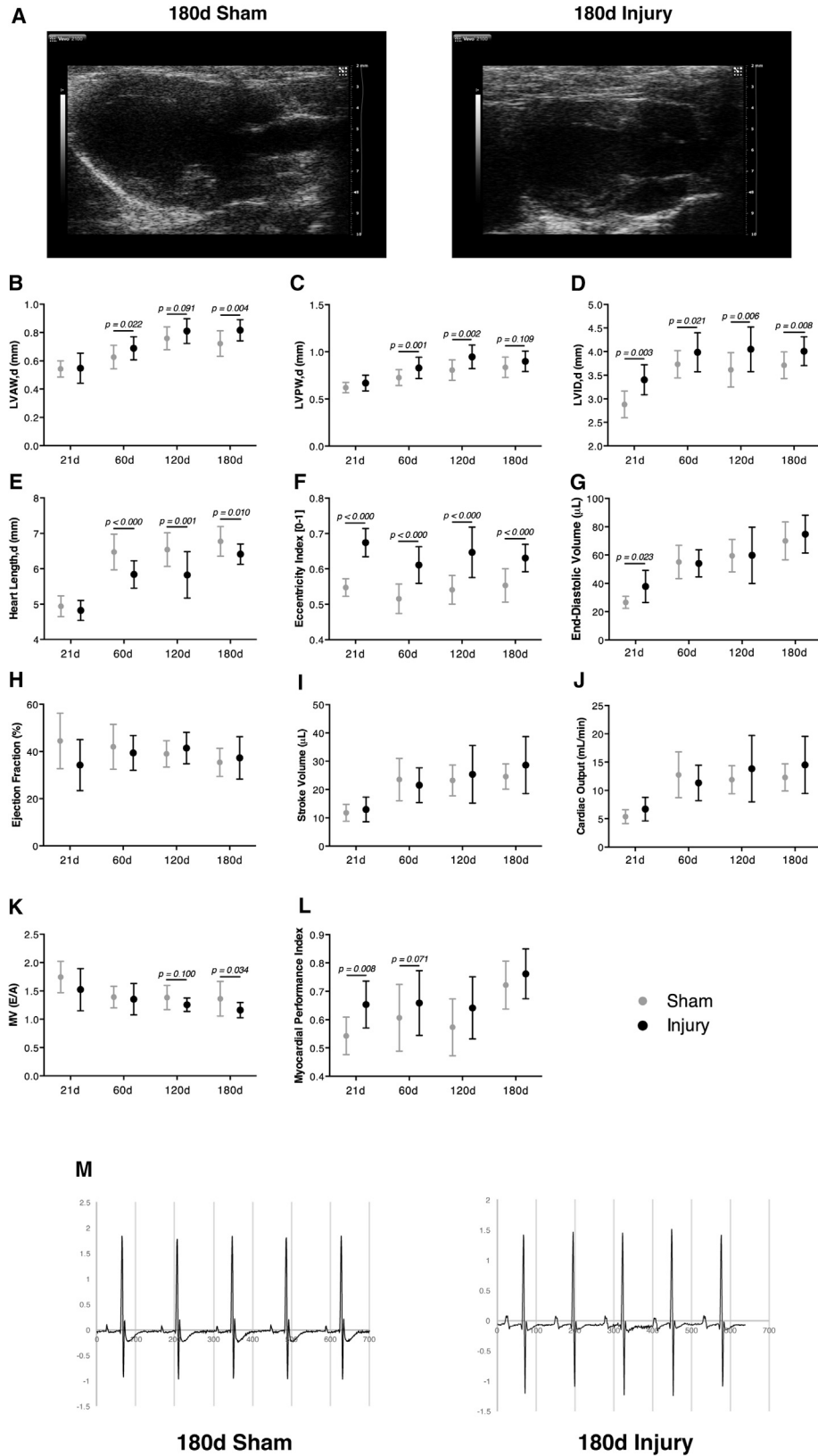
(legend on next page)

Because LV enlargement is concurrent to a reduction in heart length (Figure 2E), the eccentricity index of injured hearts was significantly increased (Figure 2F). End-diastolic volume of injured hearts was increased at 21 days, but normalized from 60 days onward (Figure 2G). Importantly, no differences were detected in the ejection fraction (Figure 2H), stroke volume (Figure 2I) or cardiac output (Figure 2J) across groups, thus showing that the systolic function of injured hearts was not significantly impaired. Regarding diastolic function, the ratio between LV early (E) to late (A) filling velocities was marginally decreased at 180 days, suggesting that incomplete relaxation and increased filling pressures might be present in resected hearts (Figure 2K). This can be explained by increased myocardial stiffness caused by the scarring, wall thickening, and/or alterations in ventricular chamber geometry. Accordingly, myocardial performance index (also known as Tei index), which comprises both systolic and diastolic parameters, showed a tendency to be increased in resected hearts (Figure 2L) at the expense of longer relaxation times (data not shown). Electrocardiogram (ECG) tracing of injured hearts was similar to control animals (Figure 2M), which was confirmed by the absence of any significant modification in the evaluated ECG parameters (Table S1).

These findings demonstrate that, despite consistent LV chamber enlargement and wall thickening, accompanied by a reduced heart length, resected hearts are functionally competent.

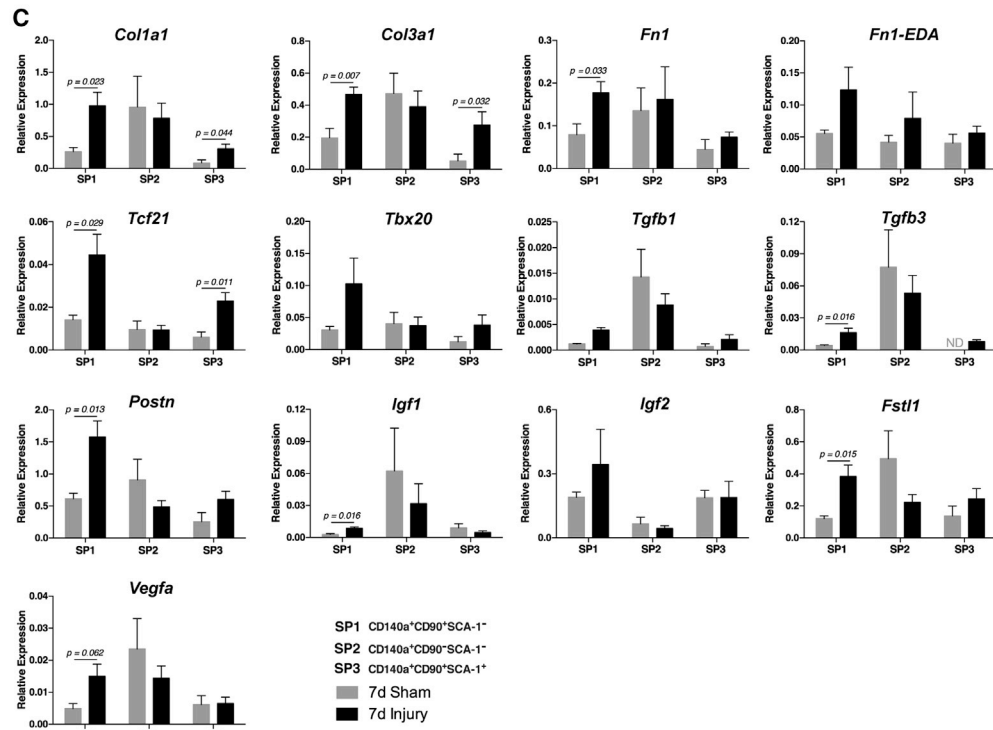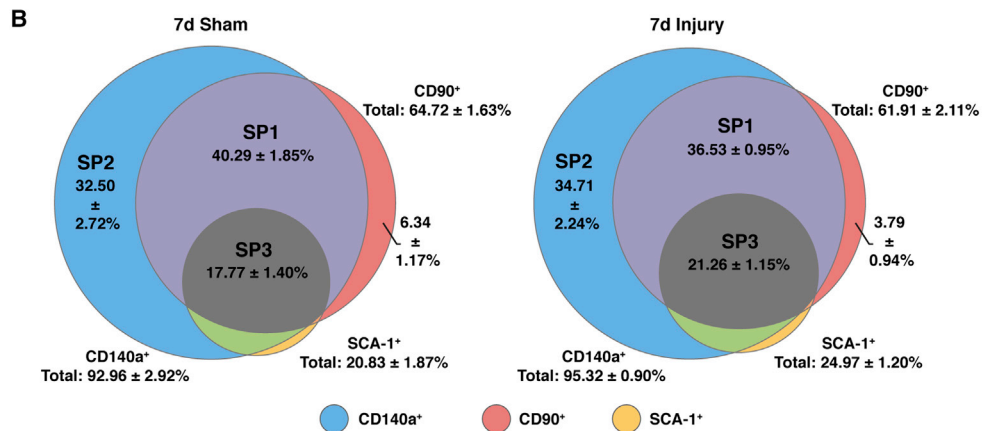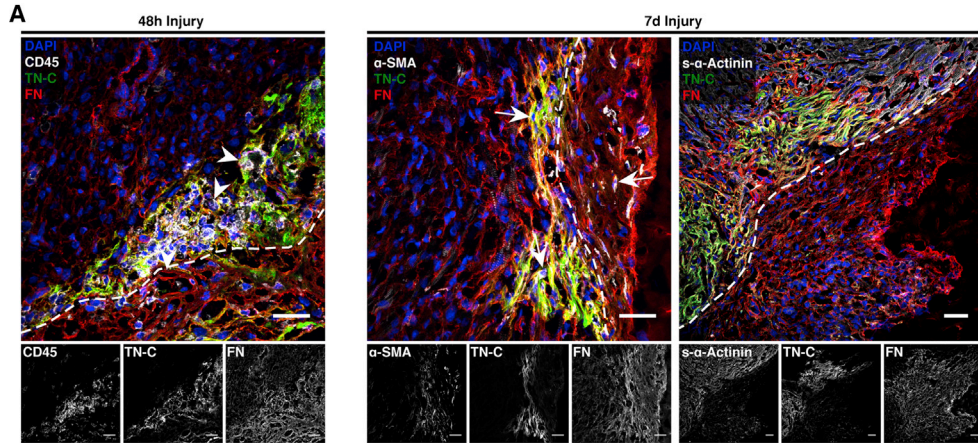## Short-Term Response to Cardiac Injury Involves Extracellular Matrix Remodeling and Fibroblast Activation

Apex amputation was evident by the disruption of the expression pattern of sarcomeric-α-actinin (s-α-Actinin) and laminin (LN) (Figure S2). Forty-eight hours after resection, the apex region was marked by the deposition of fibronectin (FN) and tenascin-C (TN-C), and by an abundant CD45$^+$ immune cell infiltrate (Figures 3A and S2, arrowheads). Myofibroblasts (α-SMA$^+$ cells) also started to appear at the injury site at this point (Figure S2, arrows). Resolution of the inflammatory phase was evident at 7 days post-injury, whereas myofibroblasts became more frequent (Figures 3A and S2). At 21 days post-resection,

α-SMA was restricted to smooth muscle cells in vessels, as observed in sham hearts. Of note, TN-C remained elevated in the border between the resection and the adjacent myocardium (Figure S2). Confocal microscopy analysis further showed that FN and TN-C were produced by CD45$^+$ hematopoietic cells during the inflammatory phase (48 hr post-surgery) and by α-SMA$^+$ myofibroblasts during inflammatory resolution (7 days post-surgery) (Figure 3A). Although largely overlapping, TN-C expression was restricted to the interface between the healthy and damaged myocardium, whereas FN displayed a more ubiquitous deposition, suggesting different biological roles (Figure 3A).

We profiled hematopoietic cells (CD45$^+$) infiltrating the apex and remote regions by flow cytometry at 2, 5, and 7 days after surgery. Single-cell suspensions were stained with antibodies to distinguish total myeloid cells (CD11b$^+$), macrophages (CD11b$^+$F4/80$^+$), monocytes (CD11b$^+$F4/80$^-$), neutrophils (CD11b$^+$Gr-1$^+$), T lymphocytes (CD3$^+$), and B lymphocytes (CD45R$^+$) (Figure S3A). At 2 days after surgery, an influx of CD45$^+$ cells was observed in the apex, paralleled by a reduction in the remote LV (Figures S3B and S3C). The rate of hematopoietic cells in the myocardium of apex-resected hearts was comparable with those observed in sham-operated controls at 7 days post-surgery, corroborating our immunofluorescence data. The immune infiltrate was mainly composed of myeloid cells. At the initial stages of injury-response (i.e., 2 days) neutrophils, monocytes, and macrophages infiltrated the myocardium at the apex, although only macrophages remained elevated up to 5 days post-surgery. No differences were observed regarding the percentage of T lymphocytes between groups, whereas B lymphocytes were significantly decreased 2 days post-injury (Figures S3B and S3C). Additional staining of myeloid populations allowed discrimination of CD11b$^+$F4/80$^+$Ly6C^{lo} macrophages, CD11b$^+$F4/80$^+$Ly6C^{hi} macrophages, CD11b$^+$F4/80$^-$Ly6C^{lo} monocytes, and CD11b$^+$F4/80$^-$Ly6C^{hi} inflammatory monocytes, as reported previously (Aurora et al., 2014). Of note, CD11b$^+$F4/80$^+$Ly6C^{hi} macrophages and CD11b$^+$F4/80$^-$Ly6C^{hi} monocytes were predominantly increased at the injury site, but not in the remote myocardium, during early inflammatory response (Figure S3D). In

Figure 2. Injured Hearts Display Morphological Alterations but Exhibit Normal Systolic Function
(A) Representative echocardiographic parasternal long-axis view 180 days post-surgery.
(B–G) End-diastolic left ventricle anterior wall thickness (LVAW), left ventricle posterior wall thickness (LVPW), left ventricle internal diameter (LVID), heart length, eccentricity index, and heart volume.
(H–J) Ejection fraction (EF), stroke volume and cardiac output determined by Simpson's method.
(K and L) Ratio between left ventricular early (E) to late (A) filling velocities and myocardial performance index (also known as Tei index) (from left to right, n = 7, 9, 22, 24, 18, 15, 18, 14).
(M) Representative ECG signal traces at 180 days post-surgery (n = 10, 6; 180 days sham, 180 days injury). See also Table S1 for detailed quantification of ECG parameters. All values are presented as means ± SD.

A

48h Injury — DAPI / CD45 / TN-C / FN

CD45 | TN-C | FN

7d Injury — DAPI / α-SMA / TN-C / FN

α-SMA | TN-C | FN

DAPI / s-α-Actinin / TN-C / FN

s-α-Actinin | TN-C | FN

B

7d Sham

SP2 32.50 ± 2.72%
SP1 40.29 ± 1.85%
CD90⁺ Total: 64.72 ± 1.63%
SP3 17.77 ± 1.40%
6.34 ± 1.17%
CD140a⁺ Total: 92.96 ± 2.92%
SCA-1⁺ Total: 20.83 ± 1.87%

7d Injury

SP2 34.71 ± 2.24%
SP1 36.53 ± 0.95%
CD90⁺ Total: 61.91 ± 2.11%
SP3 21.26 ± 1.15%
3.79 ± 0.94%
CD140a⁺ Total: 95.32 ± 0.90%
SCA-1⁺ Total: 24.97 ± 1.20%

CD140a⁺ | CD90⁺ | SCA-1⁺

C

Col1a1 — p = 0.023; p = 0.044
Col3a1 — p = 0.007; p = 0.032
Fn1 — p = 0.033
Fn1-EDA
Tcf21 — p = 0.029; p = 0.011
Tbx20
Tgfb1
Tgfb3 — p = 0.016; ND
Postn — p = 0.013
Igf1 — p = 0.016
Igf2
Fstl1 — p = 0.015
Vegfa — p = 0.062

SP1 CD140a⁺CD90⁺SCA-1⁻
SP2 CD140a⁺CD90⁻SCA-1⁻
SP3 CD140a⁺CD90⁺SCA-1⁺

7d Sham
7d Injury

(legend on next page)

turn, CD11b$^+$F4/80$^+$Ly6C^{lo} macrophages were increased at 5 days after injury, similar to what was reported following myocardial infarction at P1 (Aurora et al., 2014).

Cardiac fibroblasts are master mediators of myocardial remodeling following injury (reviewed in Souders et al., 2009). However, studies determining the cardiac fibroblast surface signature during the neonatal period are lacking. Considering the heterogeneity of this cell type, we discriminated fibroblast populations, from embryonic day 17 to adulthood (Figure S4), through the expression of the three well-reported markers of cardiac fibroblasts, i.e., CD90 (Thy-1), CD140a (PDGFRα), and SCA-1 (Furtado et al., 2014; Hudon-David et al., 2007; McQualter et al., 2009; Smith et al., 2011), following exclusion of non-viable cells (PI$^+$), endothelial cells (CD31$^+$), hematopoietic cells (CD45$^+$), and erythrocytes (TER-119$^+$). These results demonstrated that fibroblasts express the mesenchymal marker CD140a ($\geq$85%) at all stages analyzed, either in the presence or absence of CD90 (Figure S4). Throughout time these fibroblasts also acquire the expression of SCA-1 and, thus, in the adult, the most abundant subsets are CD140a$^+$CD90$^-$SCA-1$^+$ (Figure S4, green) and CD140a$^+$CD90$^+$SCA-1$^+$ (Figure S5, gray), as reported previously (Furtado et al., 2014).

We applied the same strategy to injured and sham-operated animals 7 days post-surgery (Figure 3B). Three main populations were identified: CD140a$^+$CD90$^-$SCA-1$^-$ (blue; injury: 34.71% ± 2.24%; sham: 32.50% ± 2.72%), CD140a$^+$CD90$^+$SCA-1$^-$ (purple; injury: 36.53% ± 0.95%; sham: 40.29% ± 1.85%), and CD140a$^+$CD90$^+$SCA-1$^+$ (gray; injury: 21.26% ± 1.15%; sham: 17.77% ± 1.40%). A minor population was also found expressing CD90 only (red; injury: 3.79% ± 0.94%; sham: 6.34% ± 1.17%), whereas SCA-1 was mainly confined to cells also expressing the other surface markers (Figure 3B). No statistically significant differences were detected in the relative percentages of each population between injured animals and sham-operated controls (Figure 3B). This might be explained by the use of the whole heart and/or by variability created during the isolation procedure, which may mask small differences in cell numbers in the apex. Indeed, immunofluorescence results showed a fibroblast-mediated response

to injury largely confined to the lesion site (Figures 3A and S2).

The activation of most abundant populations was assessed by real-time qPCR (sorting strategy detailed in Figure S5). The CD140a$^+$CD90$^+$SCA-1$^-$ (purple, SP1) subpopulation, which is particularly frequent in earlier developmental periods (Figure S4), responded to apex resection by upregulating genes associated with scarring (*Col1a1, Col3a1, Tgfb1,* and *Tgfb3*), CM proliferation (*Fn1, Tbx20, Igf1, Igf2,* and *Fstl1*), and neovascularization (*Vegfa*) (Figure 3C). In contrast, CD90$^+$CD140a$^+$SCA-1$^+$ (gray, SP3) cells, a subpopulation upsurging after birth (Figure S4), shows a repair-associated phenotype, with increased expression of *Col1a1, Col3a1, Tgfb1,* and *Tgfb3* (Figure 3C). CD140a$^+$CD90$^-$SCA-1$^-$ (blue, SP2) cells, more frequent in earlier developmental periods (Figure S4), were not responsive to injury, although they exhibited high expression levels of most evaluated transcripts (Figure 3C). These findings indicate that development-associated fibroblasts support the regenerative response, whereas fibroblast subsets abundant in adulthood signal mostly toward scar formation.

CM Proliferation Is Induced upon Cardiac Injury and Leads to Newly Formed CMs

The activation of CM proliferation after apex resection has been a matter of intense debate (Zebrowski et al., 2016). At 7 days post-injury, immunostaining for histone H3 phosphorylated at serine 10 (PH3) and s-α-Actinin highlighted cycling CMs that were distributed throughout the myocardium. Quantification of PH3$^+$ CMs in the myocardium below the papillary muscle and in isolated CMs from the same region showed that injured hearts displayed increased rates of mitotic CMs (PH3$^+$) in comparison with sham-operated hearts (Figures 4A and 4B). Moreover, CMs undergoing mitosis show sarcomere disruption, which is essential for effective cell division (Figures 4C and S6A; Movies S1, S2, and S3). These findings were further supported by a significant increase in CMs displaying Aurora B kinase in the nucleus and in the cleavage furrow, of the border zone and remote myocardium, of resected hearts, indicating efficient cytokinesis (Figures 4D

Figure 3. Apex Resection Triggers Local ECM Remodeling and Fibroblast Activation

(A) Representative confocal images of CD45/TN-C/FN, α-SMA/TN-C/FN, and s-α-Actinin/TN-C/FN immunolabelling at the injury site 48 hr (n = 4) and 7 days post-surgery (n = 4). Arrowhead, CD45$^+$ hematopoietic cells; arrows, α-SMA$^+$ myofibroblasts; dashed segment, resection line. Scale bars, 30 μm. See also Figure S2 for detailed analysis of cellular and extracellular matrix (ECM) remodeling following injury.

(B) Cardiac fibroblasts were isolated and prospectively identified by CD140a, CD90, and SCA-1 expression throughout ontogeny (see Figure S4), 7 days post-resection (n = 3) and sham surgery (n = 6). CD140a$^+$CD90$^+$SCA-1$^-$ (purple/SP1), CD140a$^+$CD90$^-$SCA-1$^-$ (blue/SP2), and CD140a$^+$CD90$^+$SCA-1$^+$ (gray/SP3) fibroblasts were FACS-sorted (see Figure S5 for sorting strategy).

(C) Transcriptomic profiling of SP1 to SP3 subpopulations isolated from injured (n = 5) and sham hearts (n = 4) was performed by real-time qPCR. Expression levels were normalized against *Gapdh*. All values are presented as means ± SEM. See also Figures S4 and S5 for detailed phenotypic characterization of cardiac fibroblasts throughout ontogeny and sorting strategy, respectively.
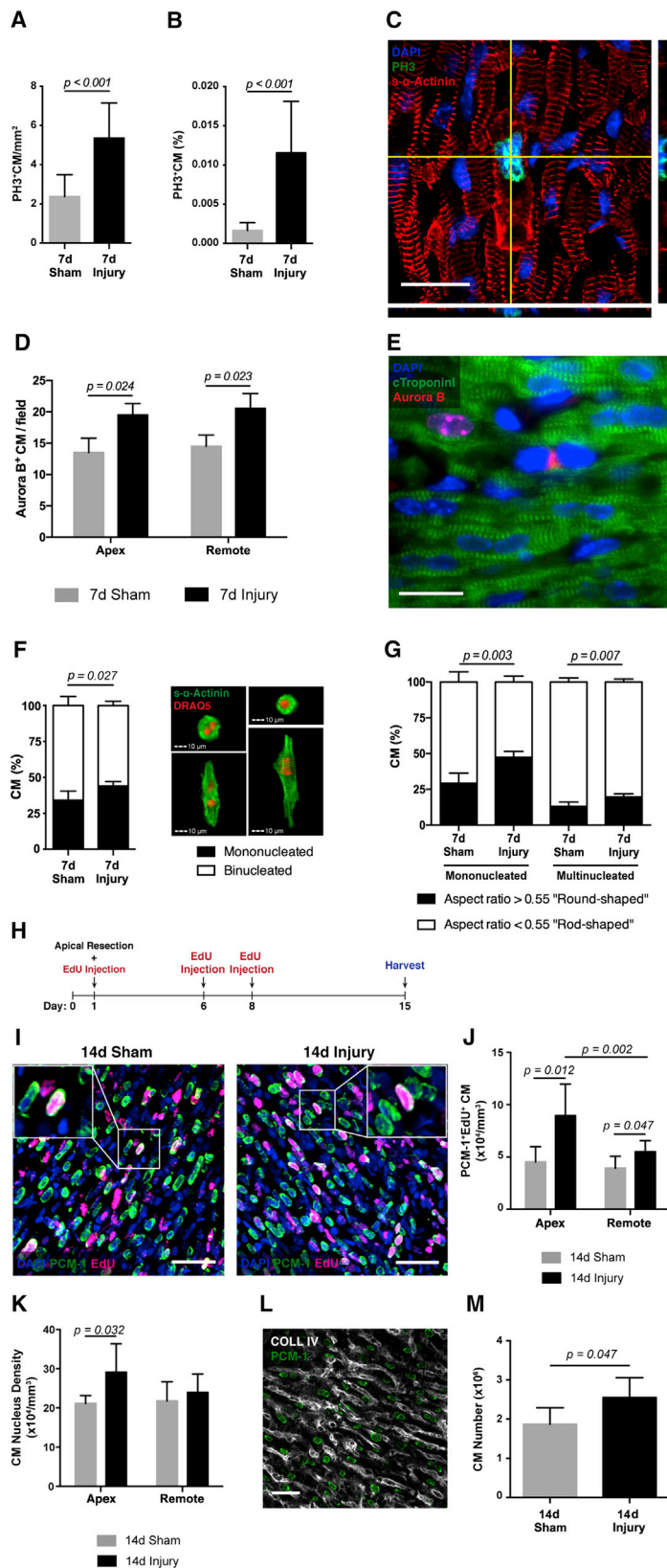
Figure 4. Activation of CM Proliferation and Not Binucleation Generates a Heart with Increased CM Number upon Apex Resection

(A and B) Quantification of PH3 expression by CMs in the area between papillary muscles and the apex (A) (n = 10, 10; 7 days sham, 7 days injury) and of isolated CMs from the same region (B) (n = 12, 11; 7 days sham, 7 days injury).

(C) Representative confocal image and respective orthogonal views of a CM expressing PH3 and clearly displaying sarcomere disassembly. Scale bar, 20 μm. See also Movies S1, S2, and S3.

(D) Quantification of Aurora B expression in CMs in regions close to the apex and remote myocardium (n = 3, 3; 7 days sham, 7 days injury).

(E) Representative image of Aurora B expression in proliferating CMs at 7 days post-surgery (n = 3). Scale bar, 20 μm.

(F) Assessment of CM nucleation in the apex region at 7 days post-surgery and representative images (n = 5, 4; 7 days sham, 7 days injury).

(G) Ratio between round-shaped (immature) and rod-shaped (mature) CMs in mononucleated and multinucleated subpopulations of CMs isolated from the apex (n = 6, 5; 7 days sham, 7 days injury).

(H) Three EdU pulses (days 1, 6, and 8) were given to trace proliferating CMs. Hearts were harvested 14 days post-surgery.

(I) Representative confocal images of PCM-1$^+$EdU$^+$ CM 14 days post-surgery. Scale bars, 40 μm.

(J) Quantification of EdU incorporation in PCM-1$^+$ CMs in the apical and remote myocardium (n = 4, 7; 14 days sham, 14 days injury).

(K) CM nucleus density at 14 days post-surgery (n = 4, 7; 14 days sham, 14 days injury).

(L) Representative confocal image of COLL IV expression in the myocardium, which allowed the delineation of CM cell boundaries and nucleation evaluation (n = 4, 7; 14 days sham, 14 days injury). Scale bar, 30 μm.

(M) Stereological estimate of the total number of CMs in the myocardium (n = 4, 7; 14 days sham, 14 days injury). All values are presented as means ± SD.

and 4E). Close to the injury, mitotic CMs were found predominantly near FN, but not TN-C. In accordance, CD29 (β1 integrin), which forms an integral part of several integrins involved in cell-matrix interactions, was found in most CMs (Ieda et al., 2009) (Figure S6).

The loss of CM proliferative potential is commonly attributed to the progression to a terminally differentiated phenotype characterized by the presence of a mature sarcomeric apparatus and binucleation (Collesi et al., 2008). To assess whether increased rates of mitosis correlated with higher rates of CM proliferation rather than multinucleation, we assessed the number of nuclei and morphometric parameters of CMs isolated from the apex by imaging flow cytometry. Injured hearts showed less multinucleation and a significant increase of mononucleated and round-shaped CMs, attesting successful cell-cycle progression and cell division (Figures 4F and 4G).

Next, we applied stereology to establish whether the proliferative upsurge observed upon apex resection impacts on total CM numbers. The mice were treated with the thymidine analog 5-ethynyl-2′-deoxyuridine (EdU), and the frequency of EdU incorporation in thick tissue sections was determined by co-labeling with PCM-1, a marker of CM nuclei (Figure 4H). The number of EdU$^+$ CMs was greater in resected hearts relative to sham-operated controls (Figures 4H–4J), further supporting an increment in CM proliferation after injury. Although CM proliferation was observed throughout the LV, the frequency of EdU$^+$ CMs was more pronounced in regions proximal to the apex, compared with remote regions (Figure 4J). In accordance, the density of myocyte nuclei was found to be significantly increased in the apex regions (Figure 4K). Combination of collagen type IV (COLL IV), to delineate cell boundaries, with PCM-1 immunolabelling, showed that CM binucleation in injured (95.7% ± 0.93%) and sham-operated hearts (95.98% ± 0.86%) was similar at 14 days after surgery (Figure 4L).

Taking multinucleation into account, we determined the density of CMs in the tissue. The volume of the LV was calculated based on morphometric analysis of longitudinal tissue sections (Figure S1A) and corrected for tissue shrinkage during fixation and processing for paraffin embedding. The total number of LV CMs in resected hearts, calculated based on CM density in the remote region, was significantly higher relative to sham-operated controls (Figure 4M). These findings show that the injury-activated CM proliferation burst, although more abundant in the apex, is also extended to remote regions, overcompensating the amount of CM loss after resection.

Resected Hearts Display Increased Capillary Density and No Signs of CM Hypertrophy or Edema

To evaluate the status of the capillary network, endothelial cells (CD31$^+$) were quantified 60 days after surgery.

The number of CD31$^+$ endothelial cells was significantly increased in injured hearts in comparison with sham-operated animals both in the apex and in the remote myocardium (Figures 5A and 5B).

To further establish whether hypertrophy was also contributing for LV wall expansion, CM size was assessed in tissue sections and isolated CMs. No significant alterations were detected in the cross-sectional area of CMs over time and in different ventricular regions, apart from the vicinity of fibrotic tissue, where CMs had a larger cross-sectional area at 180 days post-surgery (Figures 5C and 5D). Corroborating these findings, no significant differences were found in the area and volume of isolated CMs, suggesting that this hypertrophic behavior is residual and mainly localized in the apex (Figures 5E–5H). Furthermore, as edema could also explain the increase in myocardial volume, through the accumulation of fluid in the extracellular interstitial space, we examined the myocardial water content at 180 days post-surgery, but no differences were detected between the two groups (Figure 5I). Overall, these results further support that the LV wall thickening in resected hearts results from an increase in the number of CMs and is thus a consequence of injury-activated proliferation.

DISCUSSION

Sadek and colleagues reported that apex-resected murine hearts at P1 displayed regenerative capacity (Porrello et al., 2011). Others have thereafter described a lack of histological restoration, with formation of a fibrotic scar, ultimately leading to LV dilation and reduced systolic function (Andersen et al., 2014a, 2016). We performed a detailed evaluation of cellular and histo-functional alterations up to 180 days after resection and showed a well-orchestrated response in which a combined action of regenerative and reparative mechanisms is triggered, culminating in myocardial growth alongside fibrosis deposition in the innermost part of the apex. Therefore, our results are neither compatible with full regeneration (Porrello et al., 2011) nor exclusively with repair (Andersen et al., 2014a, 2016), rather showing an intermediate response which likely explains the opposing reports in the field.

As previously debated, the methodology employed during surgery and in the assessment of the extent of regeneration is determinant for obtaining reliable results and outcomes (Andersen et al., 2014b; Sadek et al., 2014). Similar to other authors (Mahmoud et al., 2014; Porrello et al., 2011), we used LV cavity exposure as a standardized method for the resection. The resultant injury, assessed by measuring the ventricular surface area, as in Porrello et al., was ~11% of the LV and therefore less severe than the 15% reported in their study.
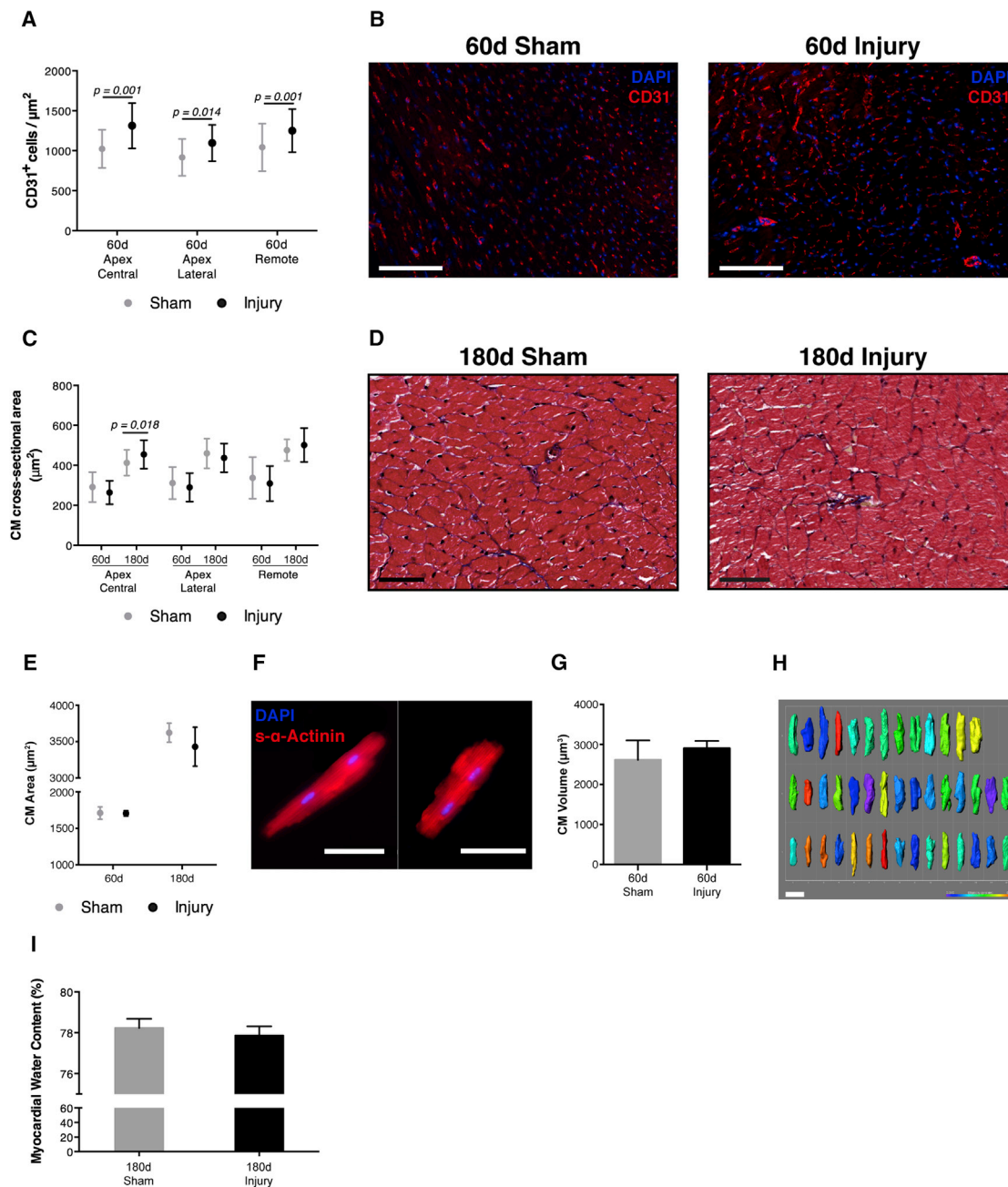
Figure 5. Resected Hearts Display Increased Coronary Vasculature but Not Hypertrophy or Edema

(A and B) Capillary density at 60 days post-surgery (i.e., number of CD31$^+$ endothelial cells per unit area) (n = 6, 7; 60 days sham, 60 days injury). Scale bars, 10 μm.

(C and D) CM cross-sectional area at 60 and 180 days post-surgery (n = 6, 6, 4, 4; 60 days sham, 60 days injury, 180 days sham, 180 days injury). Scale bars, 25 μm.

(E and F) Area of isolated CMs at 60 and 180 days post-surgery (n = 3, 5, 4, 4; 60 days sham, 60 days injury, 180 days sham, 180 days injury). Scale bar, 100 μm.

(G) Volume of isolated CMs at 60 days post-surgery (n = 4, 6 sham, injury).

(H) Representative images of 3D segmentation of CMs. Scale bars, 50 μm.

(I) Myocardial edema was assessed by myocardial water content quantification (i.e., percentage of myocardial weight that is lost after desiccation) 180 days post-surgery (n = 10, 6; 180 days sham, 180 days injury). All values are presented as means ± SD.

By quantifying (1) the incidence of sarcomere-disassembly associated with PH3, (2) EdU+ CMs in a pulse-chase experiment, and (3) Aurora B kinase in the nuclei and cleavage furrow of CMs, we showed that CMs of resected hearts exhibit increased mitotic rates, accompanied by cytokinesis. During the first week of post-natal life in mice the majority of CMs binucleate, exit from the cell cycle, and continue to grow in size (Soonpaa et al., 1996). Several lines of evidence support that proliferating CMs are mononucleated and that binucleation marks an end to cell-cycle activity during development (Bersell et al., 2009; Paradis et al., 2014). By analyzing isolated CMs by imaging flow cytometry we found that, 7 days following apex resection, CM binucleation is reduced and accompanied by an increase in the pool of mononucleated round-shaped CMs, further supporting that, in response to injury, CMs undergo karyokinesis and cytokinesis. At 14 days post-resection the levels of binucleation were already comparable with sham-operated animals, meaning that newly formed CMs follow a normal maturation progression. These results contrast with a decrease in CM mitotic activity after injury observed by Andersen et al., in which a single EdU injection was administered at the onset of surgery, most likely missing the CM proliferative burst. In a recent publication, apex resection was shown to promote a transient acceleration in binucleation, an event no longer noticeable at P8 (Zebrowski et al., 2017). According to this study, a lower number of CMs would be expected in hearts subjected to apex amputation, which was not addressed by the authors. Herein, total CM numbers, as estimated by stereology, were increased in resected hearts compared with sham controls, indicating that the majority of injury-induced CM cell-cycle activity results in proliferation, not binucleation. In the work by Zebrowski and colleagues, isolated CMs were identified by sarcomeres in phase contrast, an approach that may be adequate to identify mature (rod-shaped) CMs, but is inefficient for the identification of immature (round-shaped) CMs with less-developed sarcomeres. By bypassing the use of a CM-specific marker, the authors most likely overestimated binucleation, particularly in resected hearts, which display, according to our results, higher rates of round-shaped mononucleated CMs.

Cardiac fibroblasts are typically activated following injury, and their role in directing pathological disease remodeling is well recognized. Nonetheless, while adult fibroblasts induce hypertrophy, fetal fibroblasts promote CM proliferation and thus contribute to ventricular chamber enlargement in late development (Ieda et al., 2009). By combining the expression of three cell surface markers, we discriminated the main fibroblast subsets at different developmental stages and after cardiac injury. In response to injury, the fibroblast population, abundant at younger ages (CD140a⁺CD90⁺SCA-1⁻), upregulated genes associated with the production of extracellular matrix, neovascularization, and secreted factors known to activate CM proliferation. In contrast, the fibroblast subset that is more frequent during adulthood (CD140a⁺CD90⁺SCA-1⁺) mainly upregulated transcripts associated with fibrotic mechanisms. Altogether, these findings suggest that neonatal fibroblasts may display an intermediate phenotype between fetal and adult fibroblasts, potentially able to support both fibrogenesis and regeneration.

Earlier studies on neonatal apex resection lacked functional longitudinal studies in which the same heart is analyzed over time. Herein we paralleled the histological analysis with detailed functional evaluation by echocardiography. In contrast to Porrello et al. (2011), we observed the formation of fibrotic tissue in all analyzed hearts, which, in most cases, matured to a full-thickness scar as reported by others (Andersen et al., 2014a; Bryant et al., 2015). These contrasting observations are most likely a result of incomplete histological sampling in the former study, as shown previously (Andersen et al., 2014b). In our work, we increased sampling robustness by analyzing serial sections of the whole heart. Interestingly, while the heart weight and volume increased over time, as during normal heart growth, the scar volume diminished, indicating that the affected region was at least partially replaced by new myocardium. However, injured hearts remained shorter throughout the study, and thus the removed apex was not fully restored.

Andersen et al. (2016) performed a long-term analysis of ventricular function, using F-18-fluorodeoxyglucose positron emission tomography (FDG-PET). In this study, abnormal systolic function, short-axis enlargement and local wall thinning were demonstrated in resected hearts 180 days post-surgery, leading to the conclusion that animals developed dilated cardiomyopathy. Herein, although a tendency for reduced systolic function was evident 21 days post-surgery, no statistical differences were observed between groups over 180 days, indicating that injured hearts became functionally competent at the systolic level. Widening of resected hearts occurred through chamber expansion and LV wall thickening, which is not compatible with dilated cardiomyopathy, rather resembling an eccentric hypertrophy phenotype. The distinct results obtained from our work and Andersen et al. (2016) may reflect differences in the methodology used. While FDG-PET is particularly valuable for assessing metabolic activity, the spatial resolution of the equipment (~1 mm) falls short to precisely quantify LV wall thickness compared with the high-resolution echocardiography (~50 µm) (Gargiulo et al., 2012) used in our study. Moreover, a reduction in wall thickness was only significantly different in 1 of the 20 analyzed ventricular segments, which hardly explains a
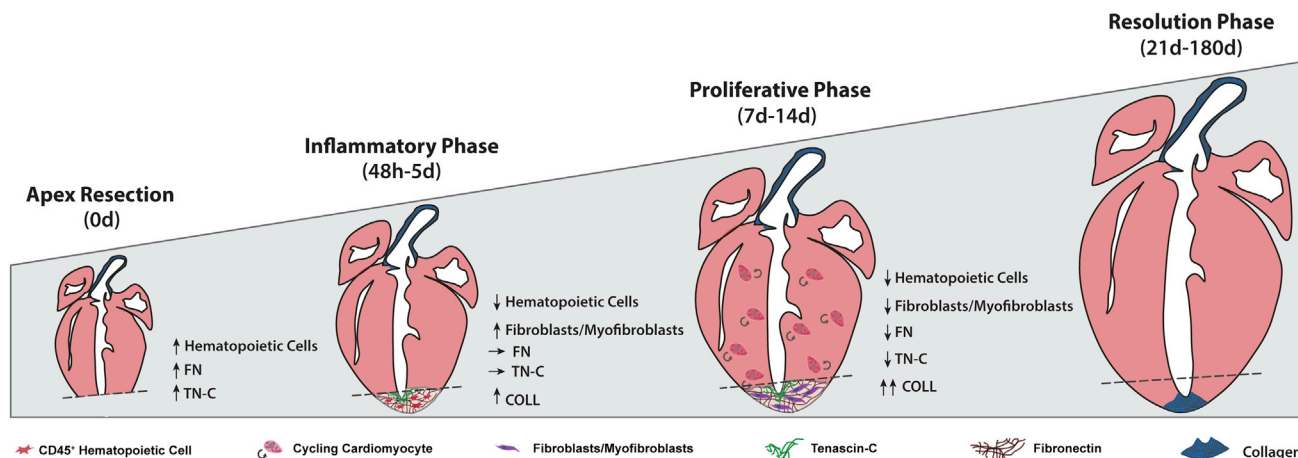
Figure 6. Proposed Model of the Biological Response Elicited by Neonatal Apex Resection

Apex resection promotes local infiltration of inflammatory cells in the first 48 hr, which leads to the deposition of a transient FN and TN-C-rich ECM. At 7 days post-injury, rates of CM proliferation are increased throughout the left ventricular myocardium and cardiac fibroblasts are activated at the injury site. These cellular dynamics result in a thickening of left ventricle walls, *de novo* vessel formation and deposition of a permanent fibrotic scar at the midpoint of the injured area. Long-term evaluation showed preserved systolic function, shortened long-axis and thicker left ventricle, without hypertrophy and edema.

dilated cardiomyopathy phenotype. The authors also missed to demonstrate progressive loss of function, typically found in small animal models of this disease (Camacho et al., 2016).

Pertinent questions have been recently raised regarding the value of neonatal apex resection to identify factors important for adult heart regeneration/repair. Although we cannot put forward conclusions on the response elicited by other injury models, our results indicate that P1 hearts subjected to mechanical trauma are capable of undergoing neomyogenesis and neovascularization, despite local fibrosis (Figure 6). In our view, these findings endorse this injury model as particularly valuable for studies aiming to block fibrosis, in favor of conditions stimulating CM proliferation and functional cardiac regeneration.

EXPERIMENTAL PROCEDURES

Supplemental Experimental Procedures are available with a detailed description of our experimental procedures.

Animals and Apex Resection Injury Model

All animal work was approved by the IBMC-INEB (Instituto de Biologia Molecular e Celular–Instituto de Engenharia Biomédica) Animal Ethics Committee, and by the Direcção Geral de Veterinária (permit 022793), and is in conformity with Directive 2010/63/EU. Humane endpoints were followed in accordance with the OECD Guidance Document on the Recognition, Assessment, and Use of Clinical Signs as Humane Endpoints for Experimental Animals Used in Safety Evaluation.

P1 C57BL/6 mice were anesthetized by hypothermia for ~3 min. Animals were laid in lateral decubitus position, the skin cut, the thorax was opened in the fourth intercostal space and the ventricular apex was resected (removing a minimal amount of tissue but ensuring lumen exposure). Subsequently, the ribs and skin were sutured and animals were exposed to heat produced by an infrared lamp to revert anesthesia and returned the progenitor. Sham-operated animals underwent the same procedure with the exception of apex resection.

Histological Characterization

At 0, 7, 14, 21, 60, 120, and 180 days after surgery, apex-resected and sham-operated hearts were harvested and processed for paraffin-embedding (see Supplemental Experimental Procedures for detailed information). Hearts were sectioned longitudinally in 3 μm sections and sampled according to Figure S1A. Subsequent histological MT staining was used to assess apex re-growth, fibrosis deposition, and injury extension.

Immunofluorescence

Immunofluorescence was performed in cryosections (0 day, 48 hr, 5 days, 7 days, 14 days, and 21 days after surgery), in histological sections (60 days post-surgery), and in cytospins of isolated CMs; as detailed in the Supplemental Experimental Procedures. Assembly, merging, and contrast/brightness adjustments were performed in Fiji v2.0.0-rc-54/.51h. software.

Flow Cytometry and Fluorescence-Activated Cell Sorting

Single-cell suspensions were prepared following digestion of cardiac tissue with crude collagenase (C2139, Sigma-Aldrich). Cells were incubated with fluorescence-conjugated antibodies or with the respective isotype controls for 30 min on ice and protected from light. Nonviable cells were excluded by adding 0.5% propidium iodide (P4170, Sigma-Aldrich) to cell suspension prior to

analysis in a FACSCanto II cytometer (BD Biosciences). Data analysis was performed in FlowJo VX software. The three most frequent fibroblast subsets were isolated by FACSAria (BD Biosciences), as described in Supplemental Experimental Procedures and in Figure S5. See also Figure S3 for detailed characterization of the inflammatory infiltrate.

Real-Time qPCR

Total RNA was isolated from FACS-sorted cells using the RNeasy Mini Kit (QIAGEN). cDNA was obtained resorting to PrimeScript RT reagent Kit (Takara) and pre-amplified using SsoAdvanced PreAmp Supermix (Bio-Rad). Real-time qPCR were performed by using iQ SYBR Green Supermix (Bio-Rad) and according to the iQ5 Real-Time PCR Detection System (Bio-Rad). Primer sequences and temperature cycles are described in Supplemental Experimental Procedures. mRNA expression was defined as primer efficiency to the power of the difference in threshold cycle values between the reference (*Gapdh*) and the genes of interest.

EdU Pulse-Chase Assay

Neonates were subcutaneously injected with 25 μg/g of animal of EdU (C10640, Sigma-Aldrich) immediately after surgery and on days 5 and 7 after surgery. Hearts were harvested at 14 days post-surgery and LV subdivided in apex and remote myocardium, each sampled in 2 mm fragments before cryosectioning (40 μm). EdU incorporation was detected using the Click-iT reaction cocktail in accordance with manufacturer instructions (C10640, Sigma-Aldrich) followed by PCM-1 immunolabelling and DAPI counterstain. Images were acquired in a Leica TCS SP5 laser scanning confocal microscope. Tissue fragments (8–10) from both regions were quantified per animal with assistance of FIJI v2.0.0-rc-54/.51h and IMARIS 8.4.1. The total number of CMs was estimated by adapting the two-step $N_V \times V_{REF}$ method (Alkass et al., 2015), where N_V is an estimate of PCM-1 density and VREF is the volume of the myocardium at 14 days post-surgery. Myocardial volume was determined by multiplying the area of the myocardium in each histological longitudinal section by the distance separating adjacent sections in 14 days post-surgery hearts. This value was corrected for tissue shrinkage during fixation and processing for paraffin embedding.

CM Isolation

CMs were isolated at 7, 60, and 180 days post-surgery. Neonatal CMs were isolated as described previously (Mollova et al., 2013), with the following alterations: CMs were fixed in 4% paraformaldehyde at room temperature (RT) for 2 hr and digested with 3 mg/mL collagenase type II (Worthington). Adult CMs were isolated by reperfusion in a Langendorff system (~80 mmHg and at 3 mL/min for 25–30 min) with Liberase TM (05401127001, Roche; 13.3 μg/mL) and Trypsin (27250018, Gibco; 13.8 μg/mL), and fixed in 4% paraformaldehyde in PBS.

Imaging Flow Cytometry

Cells were permeabilized with 1× BD Perm/Wash buffer during 15 min at RT. Incubations with primary and secondary antibodies lasted 2 and 0.5 hr on ice, respectively. Antibodies were diluted in 1× BD Perm/Wash. Immediately before acquisition in ImageStreamX cells were filtered and nuclei stained with 200 μM DRAQ5 (BioStatus).

Statistical Analysis

IBM SPSS Statistics 24 was used for statistical analysis. Shapiro-Wilk test was used to evaluate normal distribution of data. Outliers were excluded from the statistical analysis. Homoscedasticity of the sample was tested by Levene's test, which defined the statistical test(s) applied. Normally distributed and homocedastic data were tested with independent sample Student's t test and one-way ANOVA for two or three or more groups, respectively. Tukey's *post-hoc* test for correction of multiple comparisons was performed whenever significant differences were found between three or more groups.

Non-normally distributed and/or heterocedastic data were tested with Mann-Whitney U test and Kruskal-Wallis one-way ANOVA for two or three or more groups, respectively. Again, multiple comparisons were performed when three or more groups were considered statistically different. The statistical significance level chosen for all statistical tests was $p < 0.05$.

SUPPLEMENTAL INFORMATION

Supplemental Information includes Supplemental Experimental Procedures, six figures, one table, and three movies and can be found with this article online at https://doi.org/10.1016/j.stemcr.2018.01.042.

REFERENCES

Alkass, K., Panula, J., Westman, M., Wu, T.D., Guerquin-Kern, J.L., and Bergmann, O. (2015). No evidence for cardiomyocyte number expansion in preadolescent mice. Cell *163*, 1026–1036.

Andersen, D.C., Ganesalingam, S., Jensen, C.H., and Sheikh, S.P. (2014a). Do neonatal mouse hearts regenerate following heart apex resection? Stem Cell Reports *2*, 406–413.

Andersen, D.C., Jensen, C.H., and Sheikh, S.P. (2014b). Response to Sadek et al. and Kotlikoff et al. Stem Cell Reports *3*, 3–4.

Andersen, D.C., Jensen, C.H., Baun, C., Hvidsten, S., Zebrowski, D.C., Engel, F.B., and Sheikh, S.P. (2016). Persistent scarring and dilated cardiomyopathy suggest incomplete regeneration of the apex resected neonatal mouse myocardium – a 180 days follow up study. J. Mol. Cell. Cardiol. *90*, 47–52.

Aurora, A.B., Porrello, E.R., Tan, W., Mahmoud, A.I., Hill, J.A., Bassel-Duby, R., Sadek, H.A., and Olson, E.N. (2014). Macrophages are required for neonatal heart regeneration. J. Clin. Invest. *124*, 1382–1392.

Bassat, E., Mutlak, Y.E., Genzelinakh, A., Shadrin, I.Y., Baruch Umansky, K., Yifa, O., Kain, D., Rajchman, D., Leach, J., Riabov Bassat, D., et al. (2017). The extracellular matrix protein agrin promotes heart regeneration in mice. Nature *547*, 179–184.

Bersell, K., Arab, S., Haring, B., and Kuhn, B. (2009). Neuregulin1/ErbB4 signaling induces cardiomyocyte proliferation and repair of heart injury. Cell *138*, 257–270.

Bryant, D.M., O'Meara, C.C., Ho, N.N., Gannon, J., Cai, L., and Lee, R.T. (2015). A systematic analysis of neonatal mouse heart regeneration after apical resection. J. Mol. Cell. Cardiol. *79*, 315–318.

Camacho, P., Fan, H., Liu, Z., and He, J.Q. (2016). Small mammalian animal models of heart disease. Am. J. Cardiovasc. Dis. *6*, 70–80.

Collesi, C., Zentilin, L., Sinagra, G., and Giacca, M. (2008). Notch1 signaling stimulates proliferation of immature cardiomyocytes. J. Cell Biol. *183*, 117–128.

D'Uva, G., Aharonov, A., Lauriola, M., Kain, D., Yahalom-Ronen, Y., Carvalho, S., Weisinger, K., Bassat, E., Rajchman, D., Yifa, O., et al. (2015). ERBB2 triggers mammalian heart regeneration by promoting cardiomyocyte dedifferentiation and proliferation. Nat. Cell Biol. *17*, 627–638.

Darehzereshki, A., Rubin, N., Gamba, L., Kim, J., Fraser, J., Huang, Y., Billings, J., Mohammadzadeh, R., Wood, J., Warburton, D., et al. (2015). Differential regenerative capacity of neonatal mouse hearts after cryoinjury. Dev. Biol. *399*, 91–99.

Flink, I.L. (2002). Cell cycle reentry of ventricular and atrial cardiomyocytes and cells within the epicardium following amputation of the ventricular apex in the axolotl, *Amblystoma mexicanum*: confocal microscopic immunofluorescent image analysis of bromodeoxyuridine-labeled nuclei. Anat. Embryol. *205*, 235–244.

Furtado, M.B., Costa, M.W., Pranoto, E.A., Salimova, E., Pinto, A.R., Lam, N.T., Park, A., Snider, P., Chandran, A., Harvey, R.P., et al. (2014). Cardiogenic genes expressed in cardiac fibroblasts contribute to heart development and repair. Circ. Res. *114*, 1422–1434.

Gargiulo, S., Greco, A., Gramanzini, M., Petretta, M.P., Ferro, A., Larobina, M., Panico, M., Brunetti, A., and Cuocolo, A. (2012). PET/CT imaging in mouse models of myocardial ischemia. J. Biomed. Biotechnol. *2012*, 541872.

Haubner, B.J., Adamowicz-Brice, M., Khadayate, S., Tiefenthaler, V., Metzler, B., Aitman, T., and Penninger, J.M. (2012). Complete cardiac regeneration in a mouse model of myocardial infarction. Aging *4*, 966–977.

Heallen, T., Morikawa, Y., Leach, J., Tao, G., Willerson, J.T., Johnson, R.L., and Martin, J.F. (2013). Hippo signaling impedes adult heart regeneration. Development *140*, 4683–4690.

Hudon-David, F., Bouzeghrane, F., Couture, P., and Thibault, G. (2007). Thy-1 expression by cardiac fibroblasts: lack of association with myofibroblast contractile markers. J. Mol. Cell. Cardiol. *42*, 991–1000.

Ieda, M., Tsuchihashi, T., Ivey, K.N., Ross, R.S., Hong, T.T., Shaw, R.M., and Srivastava, D. (2009). Cardiac fibroblasts regulate myocardial proliferation through beta1 integrin signaling. Dev. Cell *16*, 233–244.

Jesty, S.A., Steffey, M.A., Lee, F.K., Breitbach, M., Hesse, M., Reining, S., Lee, J.C., Doran, R.M., Nikitin, A.Y., Fleischmann, B.K., et al. (2012). c-kit+ precursors support postinfarction myogenesis in the neonatal, but not adult, heart. Proc. Natl. Acad. Sci. USA *109*, 13380–13385.

Kotlikoff, M.I., Hesse, M., and Fleischmann, B.K. (2014). Comment on "Do neonatal mouse hearts regenerate following heart apex resection"? Stem Cell Reports *3*, 2.

Lavine, K.J., Epelman, S., Uchida, K., Weber, K.J., Nichols, C.G., Schilling, J.D., Ornitz, D.M., Randolph, G.J., and Mann, D.L. (2014). Distinct macrophage lineages contribute to disparate patterns of cardiac recovery and remodeling in the neonatal and adult heart. Proc. Natl. Acad. Sci. USA *111*, 16029–16034.

Mahmoud, A.I., Kocabas, F., Muralidhar, S.A., Kimura, W., Koura, A.S., Thet, S., Porrello, E.R., and Sadek, H.A. (2013). Meis1 regulates postnatal cardiomyocyte cell cycle arrest. Nature *497*, 249–253.

Mahmoud, A.I., Porrello, E.R., Kimura, W., Olson, E.N., and Sadek, H.A. (2014). Surgical models for cardiac regeneration in neonatal mice. Nat. Protoc. *9*, 305–311.

McQualter, J.L., Brouard, N., Williams, B., Baird, B.N., Sims-Lucas, S., Yuen, K., Nilsson, S.K., Simmons, P.J., and Bertoncello, I. (2009). Endogenous fibroblastic progenitor cells in the adult mouse lung are highly enriched in the sca-1 positive cell fraction. Stem Cells *27*, 623–633.

Mollova, M., Bersell, K., Walsh, S., Savla, J., Das, L.T., Park, S.Y., Silberstein, L.E., Dos Remedios, C.G., Graham, D., Colan, S., et al. (2013). Cardiomyocyte proliferation contributes to heart growth in young humans. Proc. Natl. Acad. Sci. USA *110*, 1446–1451.

Mozaffarian, D., Benjamin, E.J., Go, A.S., Arnett, D.K., Blaha, M.J., Cushman, M., Das, S.R., de Ferranti, S., Despres, J.P., Fullerton, H.J., et al. (2016). Heart disease and stroke statistics-2016 update: a report from the American heart association. Circulation *133*, e38–e360.

Paradis, A.N., Gay, M.S., and Zhang, L. (2014). Binucleation of cardiomyocytes: the transition from a proliferative to a terminally differentiated state. Drug Discov. Today *19*, 602–609.

Porrello, E.R., Mahmoud, A.I., Simpson, E., Hill, J.A., Richardson, J.A., Olson, E.N., and Sadek, H.A. (2011). Transient regenerative potential of the neonatal mouse heart. Science *331*, 1078–1080.

Porrello, E.R., Mahmoud, A.I., Simpson, E., Johnson, B.A., Grinsfelder, D., Canseco, D., Mammen, P.P., Rothermel, B.A., Olson, E.N., and Sadek, H.A. (2013). Regulation of neonatal and adult mammalian heart regeneration by the miR-15 family. Proc. Natl. Acad. Sci. USA *110*, 187–192.

Poss, K.D., Wilson, L.G., and Keating, M.T. (2002). Heart regeneration in zebrafish. Science *298*, 2188–2190.

Robledo, M. (1956). Myocardial regeneration in young rats. Am. J. Pathol. *32*, 1215–1239.

Sadek, H.A., Martin, J.F., Takeuchi, J.K., Leor, J., Nie, Y., Giacca, M., and Lee, R.T. (2014). Multi-investigator letter on reproducibility of neonatal heart regeneration following apical resection. Stem Cell Reports *3*, 1.

Smith, C.L., Baek, S.T., Sung, C.Y., and Tallquist, M.D. (2011). Epicardial-derived cell epithelial-to-mesenchymal transition and fate specification require PDGF receptor signaling. Circ. Res. *108*, e15–e26.

Soonpaa, M.H., Kim, K.K., Pajak, L., Franklin, M., and Field, L.J. (1996). Cardiomyocyte DNA synthesis and binucleation during murine development. Am. J. Physiol. *271*, H2183–H2189.

Souders, C.A., Bowers, S.L., and Baudino, T.A. (2009). Cardiac fibroblast: the renaissance cell. Circ. Res. *105*, 1164–1176.

Tidball, J.G. (2011). Mechanisms of muscle injury, repair, and regeneration. Compr. Physiol. *1*, 2029–2062.

Uygur, A., and Lee, R.T. (2016). Mechanisms of cardiac regeneration. Dev. Cell *36*, 362–374.

Zebrowski, D.C., Becker, R., and Engel, F.B. (2016). Towards regenerating the mammalian heart: challenges in evaluating experimentally induced adult mammalian cardiomyocyte proliferation. Am. J. Physiol. Heart Circ. Physiol. *310*, H1045–H1054.

Zebrowski, D.C., Jensen, C.H., Becker, R., Ferrazzi, F., Baun, C., Hvidsten, S., Sheikh, S.P., Polizzotti, B.D., Andersen, D.C., and Engel, F.B. (2017). Cardiac injury of the newborn mammalian heart accelerates cardiomyocyte terminal differentiation. Sci. Rep. *7*, 8362.

Supplemental Information

Neonatal Apex Resection Triggers Cardiomyocyte Proliferation, Neo-vascularization and Functional Recovery Despite Local Fibrosis

Vasco Sampaio-Pinto, Sílvia C. Rodrigues, Tiago L. Laundos, Elsa D. Silva, Francisco Vasques-Nóvoa, Ana C. Silva, Rui J. Cerqueira, Tatiana P. Resende, Nicola Pianca, Adelino Leite-Moreira, Gabriele D'Uva, Sólveig Thorsteinsdóttir, Perpétua Pinto-do-Ó, and Diana S. Nascimento

Fig.S1

A

40 μm (0d)
50 μm (7d)
70 μm (14d)
90 μm (21d)
130 μm (60d, 180d)

ANTERIOR

POSTERIOR

B

7d Injury

B1

7d Sham

14d Injury

B2

14d Sham

B1

B2

C

Apical Wall Thickness Occupied by Fibrosis (%)

p < 0.001
p < 0.001

7d Injury | 14d Injury | 21d Injury | 60d Injury | 180d Injury

21d Injury

Apical Wall Thickness
Occupied by Fibrosis: 46.48%

60d Injury

Apical Wall Thickness
Occupied by Fibrosis: 100%

D

HW (mg)

p = 0.006
p = 0.001
p = 0.046

7d | 14d | 21d | 60d | 180d

● Sham
● Injury

E

HW/BW (%)

p = 0.032
p = 0.003
p = 0.031

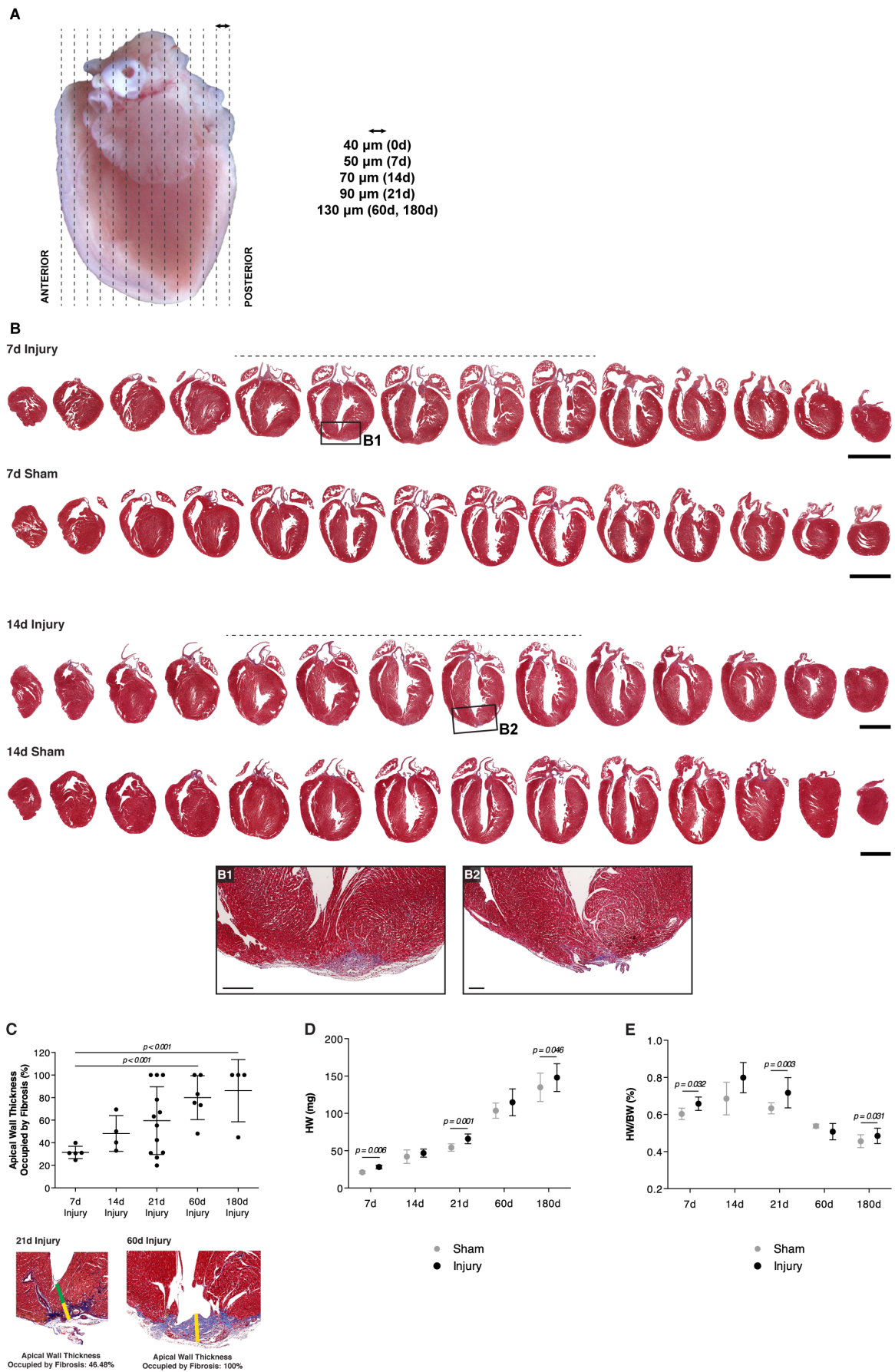7d | 14d | 21d | 60d | 180d

● Sham
● Injury

Figure S1 – Schematic Representation of Heart Sampling (Related to Experimental Procedures) & Cardiac Remodeling After Neonatal Apex Resection (Related to Figure 1)

(A) Representative sectioning was adjusted to the heart size (i.e. 40µm, 50µm, 70µm, 90µm and 130µm, between each section for 0d, 7d, 14d, 21d and 60/180d post resection, respectively), yielding approximately the same number of sections. **(B)** Representative MT stained sections of apex resected and surgical controls 7 and 14d following surgery. Sections exhibiting myocardial disruption and/or cardiac fibrosis are highlighted by a dashed line (scale bars, 2mm). High magnification images of the injury site (B1: 7d, B2: 14d) show collagen (blue staining) (scale bars, 250µm). **(C)** Percentage of left ventricle wall occupied by fibrosis in apex region was determined at 7d (n=5), 14d (n=4), 21d (n = 12), 60d (n = 6) and 180d (n = 4). **(D and E)** Heart weight (from left to right, n =4, 7, 3, 4, 8, 10, 5, 7, 19, 17) and heart to body weight ratio (from left to right, n = 4, 7, 3, 4, 8, 12, 3, 7, 19, 17). All values are presented as means ± SD.
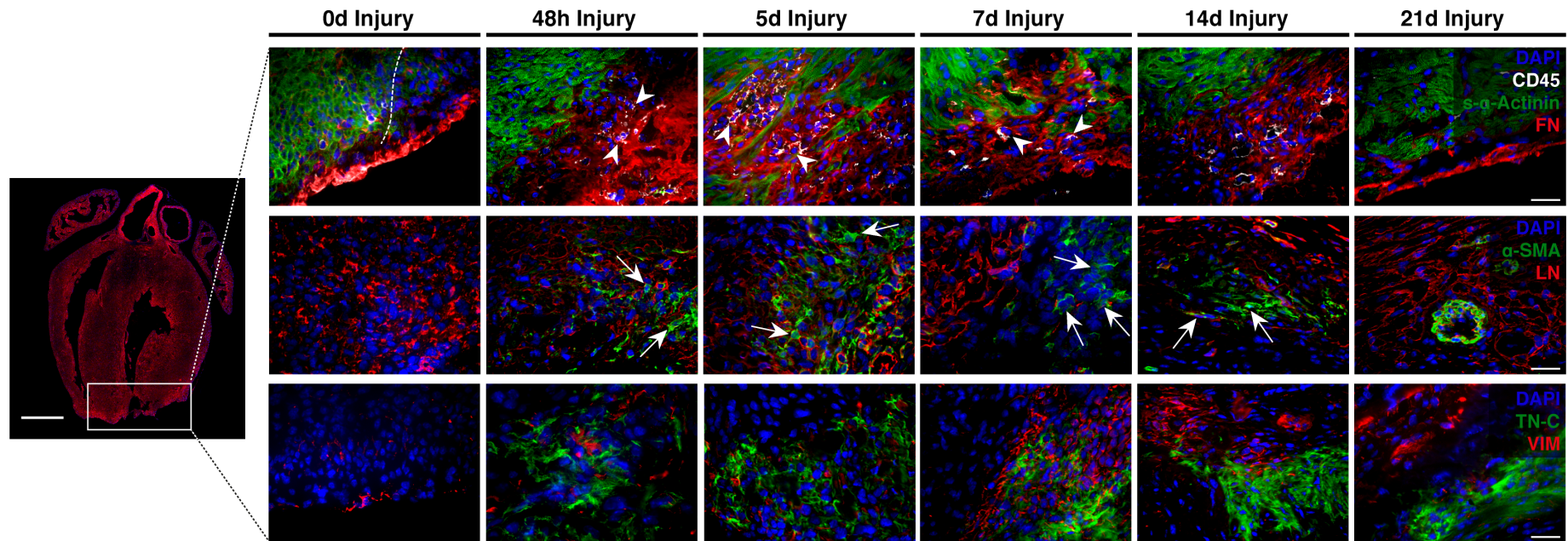
Fig.S2

Figure S2 – Time-specific Deposition of Extracellular Matrix Correlates with Cellular Dynamics (Related to Figure 2)

Arrowheads: CD45$^+$ hematopoietic cells; arrows: αSMA$^+$ myofibroblasts; Low magnification image (scale bar, 500μm), High magnification images (scale bars, 30μm) (n = 4 for each time point).

Fig.S3
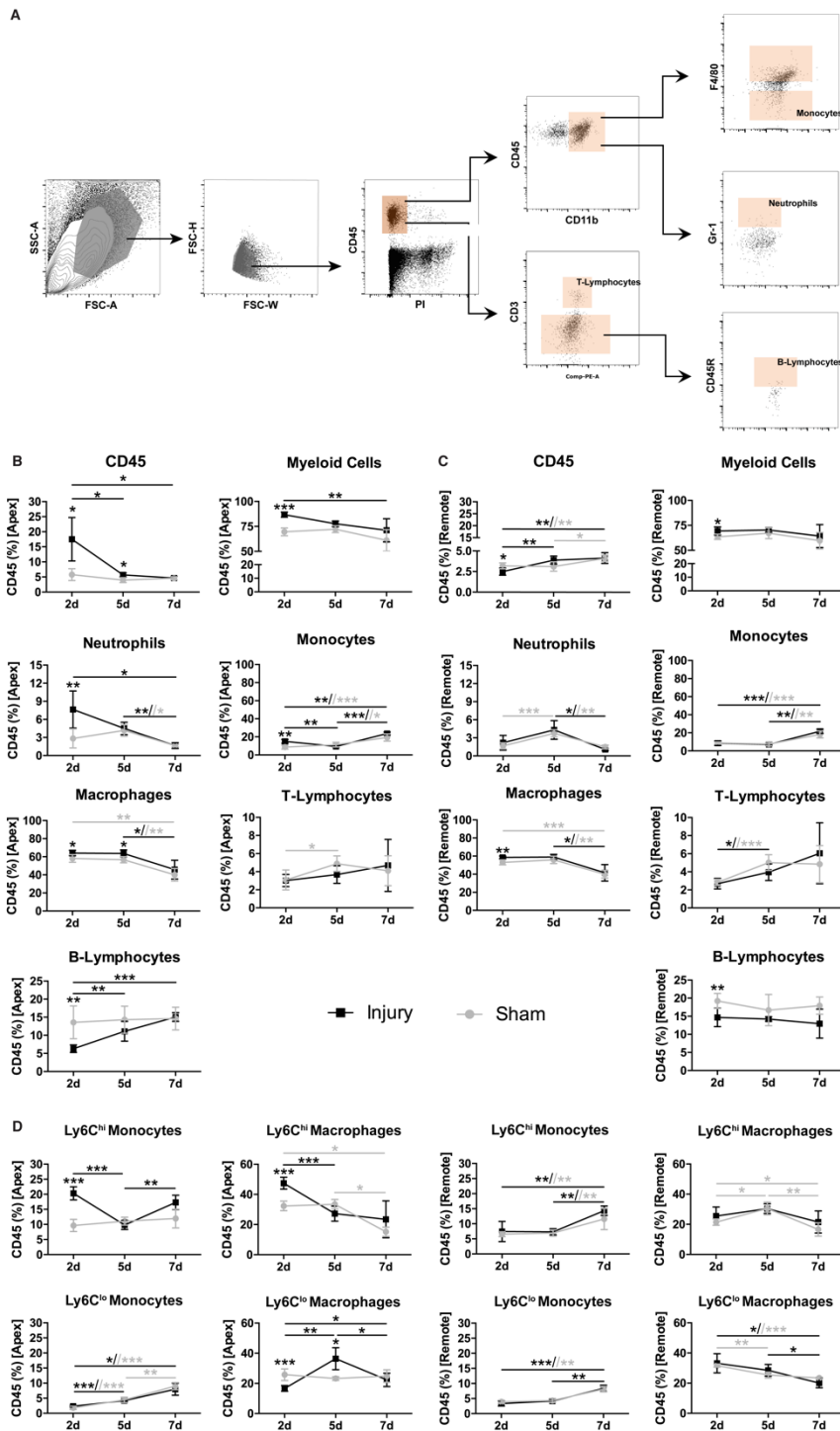
Figure S3 – Characterization of the Inflammatory Infiltrate After Injury

(A) Representative plots showing the discrimination of hematopoietic (CD45+) subsets after surgery. (B) Relative percentage of immune cell populations in the apex of apex-resected and sham-operated animals at 2d, 5d and 7d post-surgery. (C) Relative percentage of immune cell populations in the remote myocardium of apex-resected and sham-operated animals at 2d, 5d and 7d post-surgery. (D) Relative percentage of monocytes and macrophages according to Ly6C expression in the apex and remote myocardium at 2d, 5d and 7d post-surgery. (n = 7, 5, 4, 4, 3, 3; 2d sham, 2d injury, 5d sham, 5d injury, 7d sham, 7d injury). (*p<0.05; **p<0.01; ***p<0.001). All values are presented as means ± SD.

Fig.S4
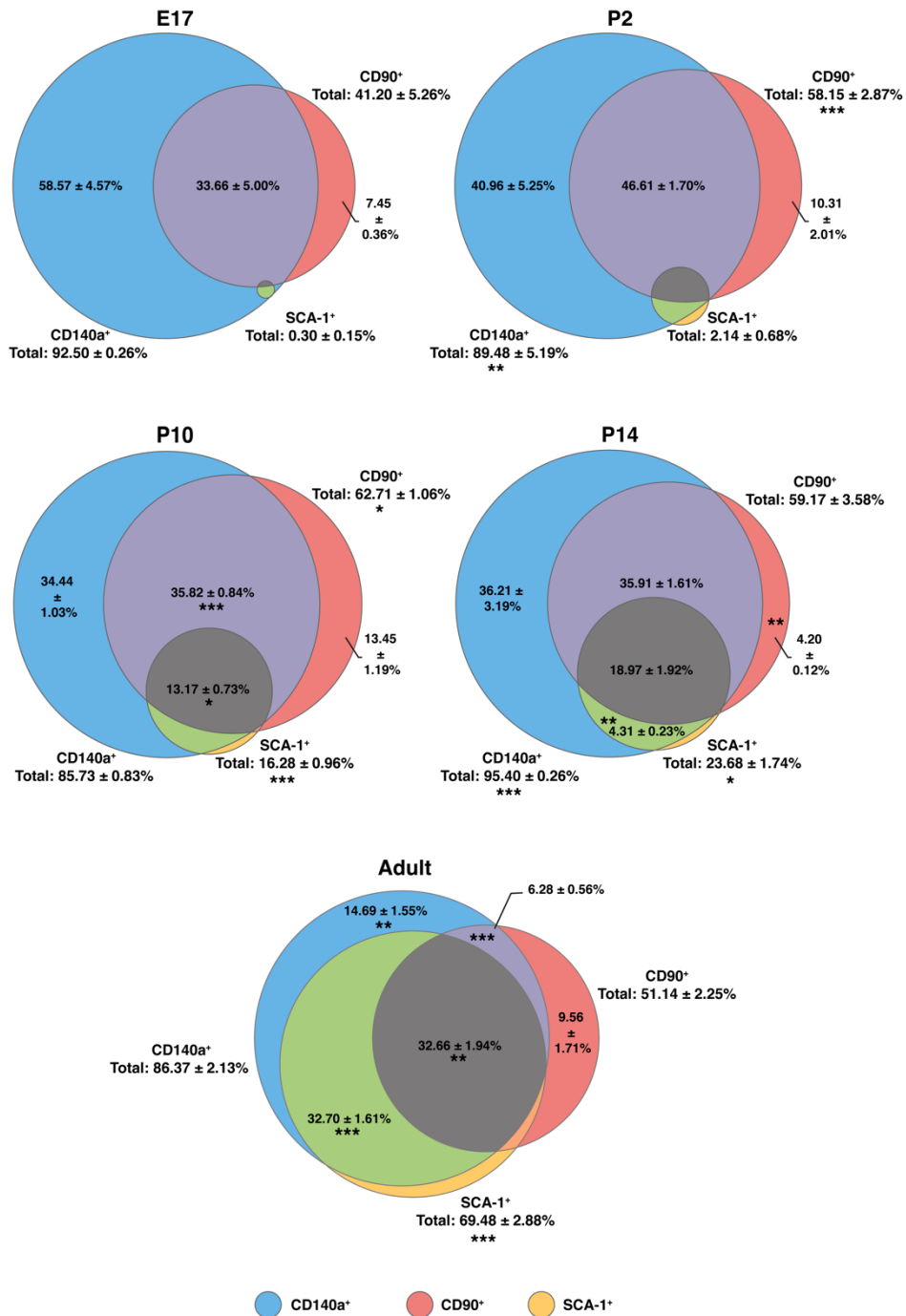
Figure S4 – Phenotypic Characterization of Cardiac Fibroblasts Throughout Ontogeny (Related to Figure 3)

Discrimination of fibroblasts based on the combined expression of CD140a, CD90 and SCA-1 at E17 (n = 2 [2 pools of 3 hearts]), P2 (n = 3), P10 (n = 3); P14 (n = 5) and adulthood (n = 4). Statistical differences (*p<0.05; **p<0.01; ***p<0.001) of each population between consecutive time points are shown. All values are presented as means ± SEM.

Fig.S5
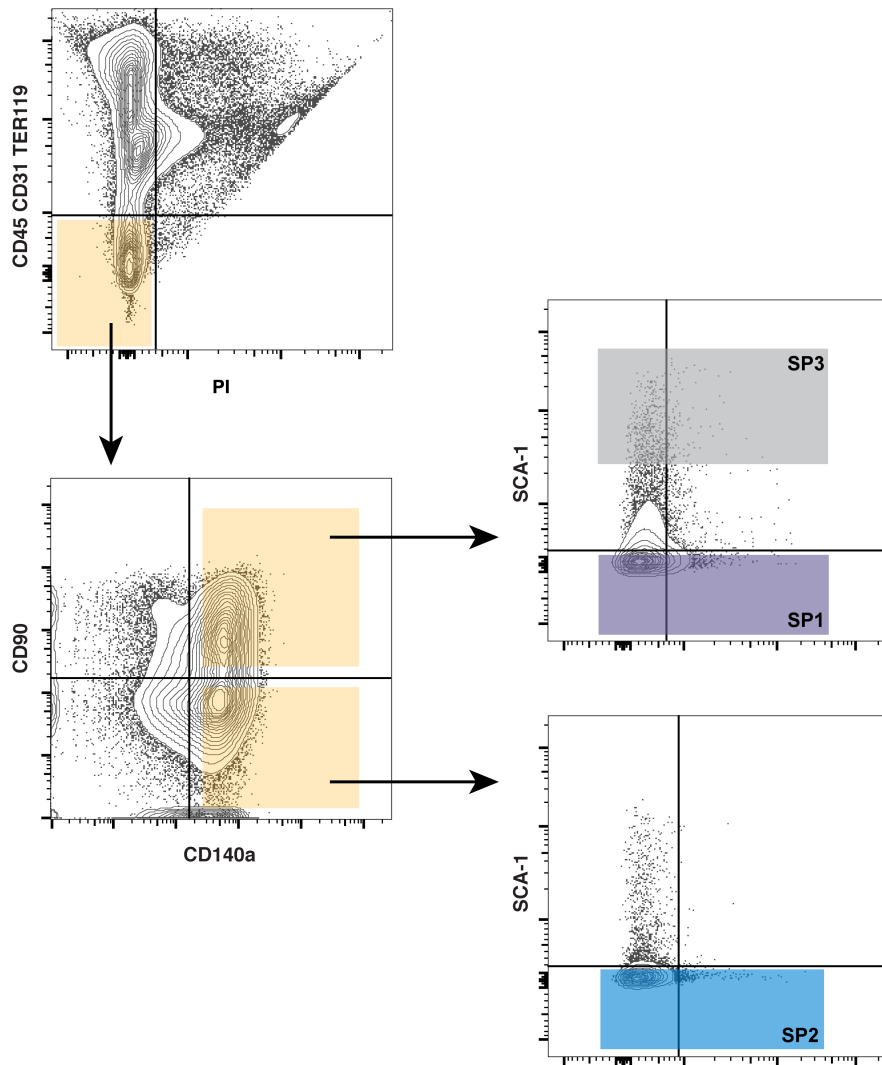
Figure S5 – Sorting Strategy to Isolate Activated Cardiac Fibroblast Populations (Related to Figure 3)

SP1, SP2 and SP3 subsets were sorted following removal of non-viable cells (PI^{+}), hematopoietic cells (CD45^{+}), endothelial cells (CD31^{+}) and erythrocytes (TER119^{+}) (n = 5, 4; 7d sham, 7d injury).

A

B
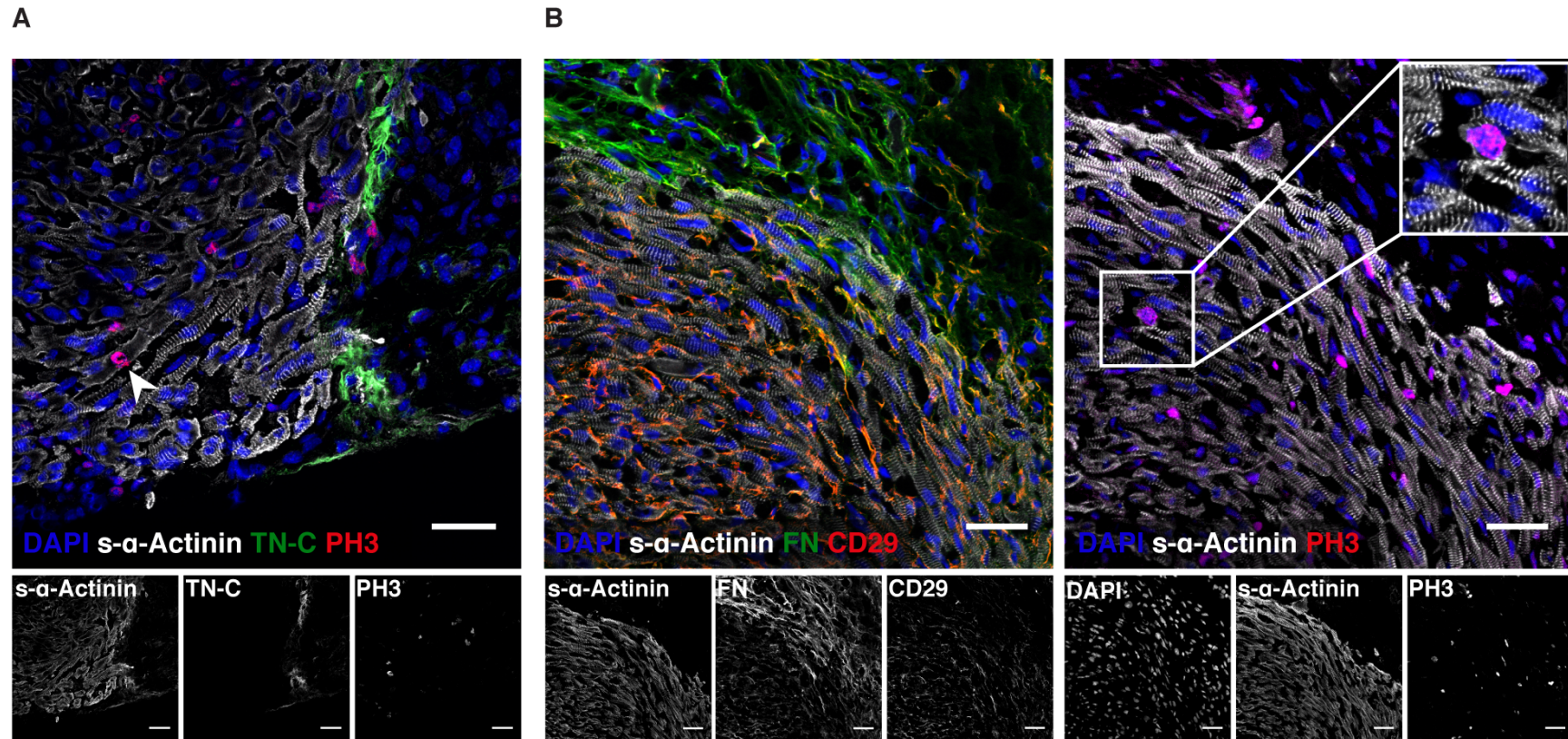
Figure S6 – CM Proliferation and ECM Production at 7d After Apex Resection (Related to Figures 3 and 4)

Representative images of consecutive sections stained for s-α-Actinin/FN/CD29 and s-α-Actinin/PH3 (n=10) at 7d post-surgery. High magnification image highlights a proliferating CMs located in a region marked by the deposition of FN and by the expression of CD29 in CMs (Scale bars, 30µm).

Table S1

Table S1 – Lead-II Electrocardiographic parameters at 180d post-surgery (Related to Figure 2)

| Variables	180d Sham (Mean ± SEM) n=10	180d Injury (Mean ± SEM) n=6	P-Value
RR Interval (s)	0,1275 ± 0,0031	0,1265 ± 0,0012	0,875 (Mann-Whitney U Test)
Heart Rate (bpm)	474,01 ± 11,34	475,02 ± 4,67	1,000 (Mann-Whitney U Test)
PR Interval (s)	0,0407 ± 0,0064	0,0442 ± 0,0020	0,065 (T-Test)
P Duration (s)	0,0143 ± 0,0008	0,0153 ± 0,0010	0,447 (T-Test)
QRS Interval (s)	0,0095 ± 0,0003	0,0093 ± 0,0034	0,928 (T-Test)
QT Interval (s)	0,0131 ± 0,0004	0,0142 ± 0,0006	0,141 (T-Test)
QTc (s)[a]	0,0367 ± 0,0014	0,0399 ± 0,0018	0,189 (T-Test)
JT Interval (s)	0,0033 ± 0,0003	0,0040 ± 0,0006	0,285 (T-Test)
Tpeak Tend Interval (s)	0,0021 ± 0,0003	0,0026 ± 0,0005	0,391 (T-Test)
P Amplitude (mV)	0,0697 ± 0,2179	0,0634 ± 0,0263	0,607 (Mann-Whitney U Test)
Q Amplitude (mV)	0,0078 ± 0,0102	-0,0552 ± 0,0238	0,056 (Mann-Whitney U Test)
R Amplitude (mV)	1,1664 ± 0,1572	1,1284 ± 0,1848	0,881(T-Test)
S Amplitude (mV)	-0,8133 ± 0,0700	-0,7484 ± 0,0863	0,374 (Mann-Whitney U Test)
ST Height (mV)	-0,0363 ± 0,0291	-0,0390 ± 0,0224	0,950 (T-Test)
T Amplitude (mV)	0,1860 ± 0,0327	0,1100 ± 0,0399	0,179 (T-Test)

[a] QT interval was adjusted to heart rate (QTc) using Bazett's formula.

s – seconds
bpm – beats per minute
mV - millivolt

Supplemental Experimental Procedures

Neonatal Apex Resection and Sham-Surgery
The neonatal injury model consists of the apex surgical resection of post-natal day (P)1 C57BL/6 mice. Animals were anesthetized by hypothermia during three minutes (min) to cease cardiorespiratory movements. Animals were laid in lateral decubitus position, exposing the left side of the flank. After immobilization with sealing tape, the skin was cut and muscle fibers disrupted until the ribs were observed. The thoracic cavity was opened in the 4th intercostal space and the left ventricle apex cut with fine scissors until chamber exposure. Thorax and skin were closed by 7-0 absorbable suture (Coated Vicryl Ethicon). Animals recovered from anesthesia under an infrared lamp and were subjected to stimulation by tightening the paw, when necessary. The surgical procedure was completed when animals regained regular breathing. Neonates were returned to the progenitor cage immediately after all the litter was intervened. During all the procedure, except throughout surgery, neonates were warmed by warming pads and infrared light. Sham mice underwent the exact same procedure with the exception of apex resection (any kind of heart manipulation whatsoever).

Histological Assessment
Hearts were harvested at 0, 7, 14, 21, 60 and 180 days post-surgery (d injury/sham). Hearts were submersed in phosphate buffer saline (PBS) and fixed in 10% formalin neutral buffer (VWR BDH & Prolabo) during 16-24 hours at room temperature (RT). For paraffin embedding, hearts were processed during a total time of 12 hours in an automated system through successive PBS washes, increasing series of alcohols (Aga), Clear Rite 3® (Richard-Allan Scientific) and Shandon Histoplast (Thermo Scientific) at 56ºC. Hearts were included in paraffin and sectioned (microtome RM2255, Leica) longitudinally (3 μm sections) according to Figure S1. Sections were dewaxed and rehydrated prior to modified Masson's Trichrome (MT) staining. The MT was performed as in the Trichrome (Masson) Stain kit (HT15-1KT, Sigma-Aldrich), with the following modifications: nuclei were pre-stained with Celestine Blue and with Gill's Hematoxylin, followed by an incubation in aqueous Bouin solution for 1 hour to promote uniform staining. Sections were diafanized in xylene and mounted in DPX Mountant for histology (06522, Sigma-Aldrich®). Images were acquired in the Hamamatsu Nanozoomer 2.0-HT digital slide scanner and subsequent editing was performed in NDP view 2 software (Hamammatsu).

Morphometric Analysis
Resorting to MT stained sections and with assistance of FIJI v2.0.0-rc-54/.51h software, morphometric analysis was performed as follows:
1. Ventricular Surface Area: measurement of the whole ventricle cross-sectional area (i.e excluding great vessels, atria and tissue adherences in the apex region);
2. Heart Length/BW: the distance between the base of the heart (region corresponding to the insertion of the great vessels in the myocardium) and the apex was normalized by the body-weight.
3. Injury (%): the percentage of sections collected from a single heart demonstrating myocardial disruption and/or fibrosis.
4. Ventricle/Scar Volume: ventricle and scarring area multiplied by the distance separating adjacent sections.
5. Apical Wall Thickness Occupied by Fibrosis (%): percentage of the left ventricle wall thickness at the apical region occupied by fibrosis.
6. Cardiomyocyte cross-sectional area: the area of transversally cut cardiomyocytes was determined in at least 30 cardiomyocytes of the apical and remote myocardium per section (at least 8 sections were analyzed per heart).

Functional Characterization
Animals at 21, 60, 120 and 180d post-surgery were subjected to echocardiography using the Vevo2100 system and a 40MHz probe (Visualsonics). Anesthesia was induced in a chamber filled with 5% isoflurane (IsoVet, Braun) and verified by loss of body posture and the paw withdrawal reflex. The animal was transferred to a heated support and the state of anesthesia was maintained through a face mask (1.5% isoflurane). Animal fur was shaved and mice paws were placed over sensors and in contact with an electric-conductive gel to monitor heart and respiratory rates. Body temperature was assessed using a rectal probe. Two-dimensional images of the heart were acquired focusing both short-axis (SAX) and parasternal long-axis (PSLAX) views. Motion-mode (M-Mode) was conducted in the SAX view to determine the thickness of LV walls as well as chamber diameter during systole and diastole. Ejection fraction (EF) was determined by Simpson's method: a longitudinal segment and three transverse segments were traced in the distal, medial and proximal region of the heart in PSLAX view, which assisted on the determination of heart volume during diastole and systole.

$$Vol_{d,s} = \frac{\left(\pi \left(\frac{[distal_{d,s}]}{2}\right)^2 + \pi \left(\frac{[medial]_{d,s}}{2}\right)^2 + \pi \left(\frac{[proximal_{d,s}]}{2}\right)^2\right) \times Heart\ Length_{d,s}}{3}$$

Stroke volume (SV) was determined by the difference between diastolic and systolic volume. Conversely, ejection fraction was determined as follows:

$$EF = \frac{SV}{Vol_d} \times 100$$

Cardiac output (CO) was calculated by multiplying SV by heart rate (HR).

Eccentricity index was determined by dividing left ventricle diameter (at the level of papillary muscles) by the longitudinal heart length (distance from the apex to great vessel insertion in the ventricle), both obtained in PSLAX during diastole.

Diastolic function was evaluated by the ratio between early (E) to late (A) filling velocities of the left ventricle.

Myocardial performance index (also known as Tei index) incorporates both systolic (IVCT - isovolumetric contraction time) and diastolic (IVRT – isovolumetric relaxation time) time intervals:

$$MPI = \frac{IVCT + IVRT}{Aortic\ Ejection\ Time}$$

By comparing these factors on sham operated and injured hearts the degree of functional restoration was ascertained.

Electrophysiological parameters were also assessed at 180d post-surgery. Anesthesia was induced and confirmed as described for echocardiographic evaluation. Animals were placed in supine position and intradermal electrodes were placed in a lead II-like configuration. ECG signals were obtained with a data acquisition hardware (PowerLab 8/35, ADInstruments) coupled to a signal amplifier (Animal Bio Amp, ADInstruments), with support of LabChart 8 software (ADInstruments).

Using an ECG analysis module RR Interval, HR, PR Interval, P Duration, QRS Interval, QT Interval, JT Interval, T-peak to T-end interval, the amplitudes of P, Q, R, S and T waves and the ST segment height were determined. Furthermore, QT corrected for the HR (QTc) was calculated through the Bazett's formula:

$$QTc = \frac{QT}{\sqrt{RR\ interval}}$$

Immunofluorescence

Both cryo and paraffin sections as well as cytospins were used to evaluate protein expression. Three μm paraffin sections were dewaxed and rehydrated by three changes in xylene, followed by sequential alcohol gradients and rinsing in deionized water. If antigen retrieval was necessary, heat-induced epitope retrieval (HIER) was applied. For HIER, sections were incubated for 35 min at 98ºC in a water bath, in 10mM Tris 1mM EDTA (Tris-EDTA), pH 9.0 and allowed to cool for 20 min at room temperature.

Tissue processing for cryosectioning involves 3 consecutive submersions (each during 24 hours at 4°C) in different solutions: 0,2% Paraformaldehyde (PFA) in 0,12M phosphate buffer (PB); 4% sucrose in 0,12M PB and 15% sucrose in 0,12M PB. A fourth incubation is performed in 15% sucrose and 7,5% gelatin in 0,12M PB during 1 hour at 37°C. Hearts were transferred to molds containing the last solution (warmed) and placed on top of dry-ice-chilled 2-methylbutane (GPR Rectapur, VWR). Frozen hearts were stored at -80°C before being cut from one end to the other into 5μm sections using a cryomicrotome (Microtom HM 550, Thermo Scientific).

When targeting epitopes that required cell membrane permeabilization, sections were treated with 0.2% Triton X-100 (for intracytoplasmic motifs) or with 1% Triton X-100 (for nuclear motifs) in PBS. Tissue sections were blocked for 1 hour in 4% FBS and 1% bovine serum albumine (BSA) or in 5% BSA in PBS. If the primary antibody was produced in mouse, the M.O.M.™ Immunodetection Kit (Vector Lab) was applied to enable blocking of endogenous Fc receptors that could be recognized by the secondary antibody. Incubation with primary antibody was performed overnight at 4ºC in a humidified chamber. Following the primary antibody incubation, sections were washed in PBS and then incubated with the secondary antibody (RT) during 1 hour. In order to amplify the fluorescence intensity of several antibodies, two streptavidin conjugated fluorophores were used: Streptavidin conjugated with Alexa 555 (S32355, Invitrogen), at 1:500 dilution and Streptavidin conjugated with Allophycocyanin (APC) (SA1005, Life Technologies), at 1:100 dilution. After washing, sections were mounted with Fluoroshield™ (F6182, Sigma-Aldrich), Vectashield mounting media with DAPI (H-1200, Vector) and observed/photographed either in a Zeiss Axiovert 200M inverted fluorescence microscope, in a Nikon eclipse 90i

fluorescence microscope, in a Leica TCS SP5 laser scanning confocal microscope or in GE IN Cell Analyzer 2000 High-Content Screening microscope.

Cytospin immunofluorescence was performed following heart digestion (see neonatal cardiomyocyte isolation section). Isolated cardiac cells were plated onto glass slides using cytospin (Shandon Cytospin® 4, Thermo Scientific) and spun for 5 min at 130g. Cells were permeabilized with 0.5% Triton for 7 min and washed three times in PBS with 0.2%Tween. Incubation with the primary antibody was carried out for 2 hours and the secondary antibody incubation for 30min, in the dark. Finally, nuclei were stained with DAPI for 10 min and slides mounted in a PBS glycerol solution (1:9) with 2.5% n-propyl-gallate (Sigma-Aldrich) without DAPI.

List of primary antibodies used and specification of the working dilution.

Antibody	Dilution	Reference
Sarcomeric-αActinin (Mouse IgG)	1:400	A7811, Sigma
Vimentin (Mouse IgG1/K)	1:50	MS-129-P, Thermo
CD31 (Goat IgG)	1:250 (requires HIER with Tris-EDTA, pH 9.0)	sc-1506, Santa Cruz Biotechnology
CD45 (Goat IgG)	1:100	AF114, R&D
Alpha-Smooth Muscle Actin (Mouse IgG)	1:400	A5228, Sigma
PH3 (Rabbit IgG)	1:800	#3377, Cell Signaling
Fibronectin (Rabbit IgG)	1:400	F-3648, Sigma
Laminin (Rabbit IgG)	1:400	L9393, Sigma-Aldrich
Tenascin-C (Rat IgG)	1:100	LAT-2, gift A. Sonnenberg
CD29 (Rat IgG)	1:50	14-0292, eBioscience
Collagen IV (Goat IgG)	1:100	AB769, Chemicon
Aurora-B (Mouse IgG1)	1:50 (requires HIER with Sodium Citrate acid buffer)	611082, BD Transduction Laboratories
Cardiac Troponin I (Rabbit IgG)	1:200 (requires HIER with Sodium Citrate acid buffer)	ab47003, Abcam
PCM-1 (Rabbit Polyclonal)	1:500	HPA023370, Sigma

List of secondary antibodies used and specification of the working dilution

Antibody	Dilution	Reference
Alexa Fluor 488 Donkey anti Mouse IgG	1:1000	A-21202, Invitrogen
Alexa Fluor 594 Donkey anti Mouse IgG	1:1000	A-21203, Invitrogen
Alexa Fluor 488 Goat anti Mouse IgG	1:1000	A11017, Molecular Probes
Cy3 Goat anti Mouse IgG	1:200	115-165-003, Jackson
Alexa Fluor 488 Goat anti Rabbit	1:200	111-545-003, Jackson
Alexa Fluor 488 Donkey anti Rabbit IgG	1:1000	A-11055, Invitrogen
Alexa Fluor 568 Donkey anti Rabbit IgG	1:1000	A-10042, Invitrogen
Alexa Fluor 633 Goat anti Rabbit IgG	1:1000	A21070, Molecular Probes
Biotinylated Donkey anti Rabbit IgG	1:250	A16033, Life Technologies
Alexa Fluor 568 Donkey anti Goat IgG	1:1000	A-11057, Invitrogen
Biotinylated Donkey anti Goat IgG	1:250	A16009, Life Technologies
Alexa Fluor 488 Donkey anti Rat IgG	1:1000	A-21208, Invitrogen
Alexa Fluor 568 Goat anti Rat IgG	1:1000	A11077, Molecular Probes
M.O.M. Biotinylated anti mouse Ig	1:250	MKB-2225, Vector Laboratories
Biotinylated Goat anti Rat IgG	1:200	BA-9400, Vector Laboratories

High Content Screening (HCS)

The proliferative response of neonatal murine hearts at 7d injury and (neo)vascularization at 60d injury were evaluated using IN Cell Analyzer 2000 (GE Health Care Life Sciences) with assistance of IN Cell Developer software (GE Health Care Life Sciences). This microscope allowed a complete scan of the sample and its software was used to quantify, through overlapping regions of interest (ROIs), the total number of proliferating cardiomyocytes (colocalization of DAPI, PH3 and sarcomeric-α-Actinin expression) or the total number of

endothelial cells (colocalization of DAPI and CD31 expression) per area (quantified in advance by the assembly of individual images in FIJI v2.0.0-rc-54/.51h.).

Flow Cytometric profile of Cardiac Populations and Fluorescence Activated Cell Sorting (FACS)
Flow cytometry was performed to characterize cardiac stroma, namely fibroblast populations, from E17 to adulthood and inflammatory populations 2d, 5d and 7d post-surgery. Cardiac cells were isolated by digestion of cardiac tissue fragments with crude collagenase (C2139, Sigma-Aldrich®) at 200 µg/ml concentration and DNase (A3778, VWR) at 60U/ml in Hank's balanced salt solution (HBSS) (H9269, Sigma-Aldrich®). Collagenase digestions were performed during 15 min at 37ºC until no tissue was observed by visual inspection. After each digestion, the suspension was decanted, the medium collected (cellular portion) and a new collagenase/DNase solution was added to the remaining tissue fragments. The collected cell suspension was mixed with HBSS with 10% FBS to neutralize enzymatic activity and was kept on ice. The collected cellular fraction of each digestion was combined and washed in FACS medium (0.01% sodium azide and 3% FBS in PBS). Cells were evenly distributed for each staining in a round bottom multiwell plate. Fc receptors were blocked using anti-mouse CD16/CD32 at 0.5 µg/µl in FACS medium during 20 min. After two washes in FACS media, cells were incubated during 30 min with the antibody cocktail on ice and in the dark. Cells were washed twice in FACS media and transferred to FACS tubes. In order to exclude nonviable cells from the analysis, 0.5% of propidium iodide (PI) (P4170, Sigma-Aldrich) was added to the cell suspension 1-2 min prior to analysis. Fifty thousand events (of appropriate size and complexity) per staining were acquired in the cytometer FACS Canto II (BD Biosciences). For characterization of inflammatory cells, after antibody incubation, cells were fixed in 1% PFA in FACS medium during 15 min and acquired afterwards. Subsequent analysis and graphing were performed in FlowJo VX software.

List of antibodies and isotype controls used in flow cytometry and specifications of the working dilution.

Antibody	Dilution	Reference
CD31-PeCy7 (Rat IgG2a)	1:100	25-0311-81, eBioscience
CD45-PeCy7 (Rat IgG2b)	1:100	25-0451-81, eBioscience
TER119-PeCy7 (Rat IgG2b)	1:100	116222, Biolegend
CD90.2-FITC (Rat IgG2b)	1:100	105306, Biolegend
CD90.2 PE (Rat IgG2a)	1:100	553930, BD Pharmingen
CD140a-APC (FL4) (Rat IgG2a)	1:100	135907, Biolegend
SCA-1 FITC (Rat IgG2a)	1:100	11-5981-81, eBioscience
SCA-1-PE (FL1) (Rat IgG2a)	1:100	12-5981-81, eBioscience
CD44-APC/Cy7 (Rat IgG2b)	1:50	103028, Biolegend
CD45-PE(Rat IgG2b)	1:100	12-0451-82, eBioscience
CD11b-APC (Rat / IgG2b)	1:100	17-0112-82, eBioscience
F4/80-FITC (Rat / IgG2a)	1:100	11-4801-82, eBioscience
Ly6C-PeCy7 (Rat / IgG2c)	1:100	25-5932-82, eBioscience
Gr-1-FITC (Rat IgG2b)	1:100	11-5931-82, eBioscience
CD3e-PacBlue (S. Hamster IgG2)	1:100	558214, BD Biosciences
CD45R-PeCy7 (Rat IgG2a)	1:100	25-0452-82, eBioscience
Isotype Control PeCy7 (Rat IgG2a)	1:100	400521, Biolegend
Isotype Control PeCy7 (Rat IgG2b)	1:100	400617, Biolegend
Isotype Control FITC (Rat IgG2a)	1:100	400505, Biolegend
Isotype Control FITC (Rat IgG2b)	1:100	IC013F, R&D
Isotype Control PE (Rat IgG2a)	1:100	400508, Biolegend
Isotype Control APC (Rat IgG2a)	1:100	IC006A, R&D
Isotype Control APCCy7 (Rat IgG2b)	1:100	400623, Biolegend

Real-time Polymerase Chain Reaction (qRT-PCR)

Primer sequences for qRT-PCR

Gene	Primer Sequence (5' to 3')	PCR Product Length	Annealing Temperature (°C)
Gapdh	FW: CGTCCCGTAGACAAAATGGT RV: TTGATGGCAACAATCTCCAC	110 bp	60
Col1a1	FW: GCTCCTCTTAGGGGCCACT RV: CCACGTCTCACCATTGGGG	247 bp	60
Col3a1	FW: CCTGGCTCAAATGGCTCAC RV: GACCTCGTGTTCCGGGTAT	214 bp	60
Fn1	FW: GCTCAGCAAATCGTGCAGC RV: CTAGGTAGGTCCGTTCCCACT	117 bp	60
Fn1-EDA	FW: ACTCGAGCCCTGAGGATG RV: CTGAGGCCCTGCAGCTCT	82 bp	60
Tcf21	FW: CGCTCACTTAAGGCAGATCC RV: CTGTAGTTCCACACAAGCGG	149 bp	60
Tbx20	FW: AAACCCCTGGAACAATTTGTGG RV: CATCTCTTCGCTGGGGATGAT	171 bp	60
Tgfb1	FW: CTTCAATACGTCAGACATTCGGG RV: GTAACGCCAGGAATTGTTGCTA	142 bp	60
Tgfb3	FW: GCAAGAATCTGCCCACAAGG RV: CCATTGGGCTGAAAGGTGTG	145 bp	60
Postn	FW: TGGTATCAAGGTGCTATCTGCG RV: AATGCCCAGCGTGCCATAA	135 bp	60
Igf1	FW: CACACCTCTTCTACCTGGCG RV: GTACTTCCTTCTGAGTCTTGGGC	321 bp	60
Igf2	FW: GGGAAGTCGATGTTGGTGCT RV: AAGCAGCACTCTTCCACGAT	200 bp	60
Fstl1	FW: TAATGGCGACTCTCACCTGG RV: ATGAGGGCGTCAACACAGAG	135 bp	60
Vegfa	FW: CCACGACAGAAGGAGAGCAG RV: CACTCCAGGGCTTCATCGTT	196 bp	60

Neonatal Cardiomyocyte Isolation

Seven days post-surgery neonatal hearts were harvested and cut into small fragments (approximately 2mm), before being flash frozen in liquid nitrogen until further use. Then, fragments were thawed at RT and fixed with 4% PFA in PBS for 2 hours with stirring (100 rpm). Following fixation, fragments were digested with collagenase type II (Worthington, CLS-2) (3 mg/ml in HBSS) overnight at 37°C (100 rpm) and mechanically dissociated until no fragments were detected (additional digestions were sometimes required, depending on the original size of the fragment). In order to inactivate collagenase, equal volume of HBSS with 10% FBS was added. At this stage, cells can be stored at 4°C or, alternatively, processed for cytospin immunofluorescence or for imaging flow cytometry (see Imaging Flow Cytometry). This methodology yields ~70% purity of CMs.

Imaging Flow Cytometry

Aiming at performing a morphometric characterization of cardiomyocytes, cell suspensions were centrifuged at 300g for 10min and the cellular portion was then resuspended in FACS medium (0.01% sodium azide and 3% FBS in PBS) and permeabilized with 1X BD Perm/Wash™ Buffer during 15 min at RT. Incubation with primary and secondary antibodies lasted for 2 hours and 30 min on ice, respectively. Both antibodies were diluted in 1X BD Perm/Wash™ Buffer and incubations were separated by two washes with 1X BD Perm/Wash™ Buffer at 800g. Finally, they were ressuspended in PBS and kept at 4°C until acquisition. Immediately before acquiring in Imagestream®X, cells were filtered (100μm cell strainer) and their nuclei were stained with 200 μM of DRAQ5 (5 mM, Biostatus).

Cardiomyocyte morphometric analysis was performed using IDEAS® software. This software calculates several features of CMs (area, major axis, minor axis and aspect ratio) and allows mask creation (definition of a specific area), which allows the assessment of nuclear number. Unfocused cells were promptly removed by eliminating cells with Gradient RMS smaller than 40 and debris and duplets were excluded by removing objects with a small area and high aspect ratio. Whenever the aspect ratio was smaller than 0.55, cardiomyocytes were classified as "Rod" and above this value were considered "Round".

Adult Cardiomyocyte Isolation
Adult cardiomyocytes were isolated by reperfusion of the heart in a Langendorff system with liberase TM (05401127001, Roche) at 13.3 μg/ml concentration and trypsin (27250018, Gibco) at 13.8 μg/ml concentration in a heated aqueous buffer containing: NaCl (113mM), KCl (4.7mM), $MgSO_4$ (1.2mM), Na_2HPO_4 (0.6mM), KH2PO4 (0.6mM), NaHCO3 (12mM), KHCO3 (10mM) and Taurine (30mM). Perfusion was performed under physiological pressure ($\pm$ 80 mmHg) and rate (3ml/min) and lasted for 25 to 30 min. At this point the heart appears swollen, pale and flaccid and is cut into small pieces, which are further dissociated by a plastic pipette. Digestion is halted by adding ice-chilled FBS to the buffer (final concentration 10%) and the cell suspension is filtered using a 300 μm mesh. Then CMs are fixed for 30 min with 4% PFA in PBS and stored at 4ºC in PBS with 0,1% sodium azide.
The area of adult CMs, isolated from 60d and 180d post-surgery hearts, was evaluated by immunofluorescence in cytospins.
The volume of adult CMs, isolated from 60d post-surgery hearts, was evaluated with the assistance of IMARIS 8.4.1. The surface module allowed a semi-automatic segmentation of CMs and volume determination.